Gyre-Scale Acoustic Tomography: Modeling Simulations

PAOLA MALANOTTE-RIZZOLI

Department of Earth, Atmospheric and Planetary Sciences, Center for Meteorology and Physical Oceanography, Massachusetts Institute of Technology, Cambridge, MA 02139

WILLIAM R. HOLLAND

National Center for Atmospheric Research, Boulder, CO 80307

(Manuscript received 17 May 1984, in final form 18 January 1985)

ABSTRACT

Ocean Acoustic Tomography was proposed by Munk and Wunsch as a method for making measurements of ocean variability over large areas. After the successful demonstration of the feasibility of the idea in the 1981 three-dimensional Mesoscale Experiment the tomography group has proposed a new experiment to be carried out in the Eastern Pacific Ocean, on ranges as long as the subtropical gyre scale.

This paper addresses the question of which average quantities of importance for the ocean general circulation and ocean climate can be measured by tomography and with what accuracy. The paper focusses upon the following quantities: i) measurement of the heat content vertical profile horizontally averaged over a tomographic section; ii) time variability of the average heat content, or average pycnocline displacement, at different depths; iii) measurement of the average pycnocline slope at different depths.

To answer the above question the tomographic experiment is simulated in a given model ocean, using Holland's eddy-resolving general circulation quasi-geostrophic model. The results of the modeling simulations can be summarized as follows.

i) The tomographic technique bears upon the use of inverse methods to reconstruct the interior sound speed perturbation field, or, equivalently, the heat content field. Over ranges as long as the gyre scale, the typical result of a single inversion is to provide an ocean with warm or cold biases. A simple iterative procedure allows the removal of these biases. The final estimates of the mean heat content (averaged over the tomographic section) at different depths is very good.

ii) Through a time-evolution experiment carried out for the duration of a full year, the time evolution of the average pycnocline displacement can be monitored at various depths. Thus tomography can measure the frequency spectrum of the average pycnocline displacement in layers below the surface mixed layer in which the circulation is basically wind-driven.

iii) The initial estimate of the average heat content can be significantly improved through a better specification of the statistics of the region, like the inclusion of a spatial mean in the horizontal covariance function for the sound speed perturbation. In particular, the inclusion of an inhomogeneous covariance modeling long-scale pycnocline trends allows us to estimate the average pycnocline slope at various depths. The obtained slope estimates are very good. Measurement of isopycnal slopes averaged in time could be used for β-spiral calculations. Thus, simple "density" tomography would provide a tool to evaluate the absolute velocity field and not only the geostrophic velocity shear.

1. Introduction

Acoustic tomography was proposed by Munk and Wunsch (1979) as a method for making measurements of ocean variability over large areas. The transparency of the ocean to sound propagation made it possible to contemplate exploiting systems which could take advantage of the natural integration along acoustic paths, and the geometric growth in information with the number of moorings available. The methodology proposed in the original paper relied upon the combination of recent developments in acoustic hardware with those in geophysical inverse theories. The full three-dimensional demonstration of mapping the mesoscale eddy field by tomography which took place over four months in mid-1981 in the western North Atlantic proved the feasibility of the idea. (Ocean Tomography Group, 1982; Cornuelle *et al.*, 1985). The tomography group has now moved ahead proposing a new experiment to be carried out in 1986 in the eastern part of the Pacific Ocean over ranges of the order of the subtropical gyre scale.

A general problem addressed by the recent oceanographic research deals with how to link dynamical models of the ocean general circulation with experimental data sets, in this instance tomographic data. Two steps are necessary in this process. The first step is to simulate the tomographic experiment in a given model ocean to determine which quantities can be measured and with what accuracy. The second step

is to learn how to use tomographically measured quantities to constrain the dynamical model to behave as observed in limited regions of the ocean. The purpose of imposing constraints derived from experimental data is to improve the model performance and to observe how the model properties are modified in far away, dynamically connected regions.

In this paper the first step is investigated through the simulation of the forthcoming gyre-scale tomographic experiment in the model ocean. The model is Holland's quasi-geostrophic, eddy-resolving three layer model for the subtropical gyre. As the forthcoming 1986–87 tomographic experiment will focus on "density" tomography, the present simulations are devoted to measuring the following quantities: 1) the vertical profile of heat content horizontally averaged along the tomographic section; 2) the time-variability of the average heat content, or average pycnocline displacement, at different depths; 3) the time variability of the average pycnocline slopes at different depths.

The paper is organized as follows. In section 2 we give a description of the model and a short discussion of the basic quantities measured in the tomographic simulations.

Section 3 presents the results of the simulated experiment for two long range sections chosen in the model ocean. The first one, a zonal section was chosen on the basis of its similarity in pycnocline trends with a hydrographic section measured in the Eastern Pacific by Kenyon (1983). A meridional, eastern section was also considered in the inversions. First, a brief summary is given of the successive stages of the experiment. Second, the results of the various simulations are presented.

Finally, in Section 4, we present the conclusions of the present study.

2. Tomographic measurements on the gyre scale

The model to be used for the simulation of the tomographic experiment is Holland's quasi-geostrophic, eddy-resolving general circulation model in its 3-layer version. Figure 1 shows a schematic diagram for the vertical structure of the three-layer model where $H_1 = 300$ m; $H_3 = 700$ m; $H_5 = 4000$ m are the three layer thicknesses. The ocean basin is 4000 km × 4000 km wide; is 5000 m deep; has a grid spacing $\Delta = 20$ km. The fine horizontal resolution is required by an Eddy-Resolving General Circulation Model (ERGCM) to represent the mesoscale eddy scale as well as the gyre scale.

We now give a short description of the model. Following Holland (1978) the quasi-geostrophic vorticity equations for the three layers, coupled with the two interfaces equation, can be written as:

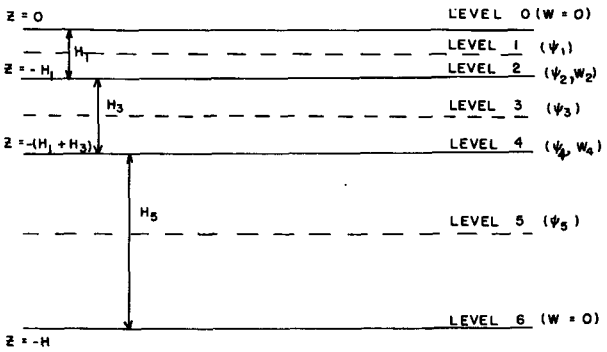

FIG. 1. Schematic diagram for the vertical structure of the three-layer eddy resolving model.

$$
\begin{aligned}
&\frac{\partial}{\partial t}\nabla^2\psi_1 = J(f+\nabla^2\psi_1, \psi_1) - \left(\frac{f_0}{H_1}\right)w_2 + F_1 + \frac{\mathrm{curl}_z\tau}{H_1}\\
&\frac{\partial}{\partial t}\nabla^2\psi_3 = J(f+\nabla^2\psi_3, \psi_3) + \left(\frac{f_0}{H_3}\right)w_2 - \left(\frac{f_0}{H_3}\right)w_4 + F_3\\
&\frac{\partial}{\partial t}\nabla^2\psi_5 = J(f+\nabla^2\psi_5, \psi_5) + \left(\frac{f_0}{H_5}\right)w_4 + F_5 + B_5\\
&\frac{\partial}{\partial t}h_2 = J(h_2, \psi_2) - w_2\\
&\frac{\partial}{\partial t}h_4 = J(h_4, \psi_4) - w_4
\end{aligned}
\qquad (1)
$$

where ψ_1, ψ_3, ψ_5 are the streamfunctions in the three vertical layers; w_2, w_4 the vertical velocities at the two interfaces; $f = f_0 + \beta y$ is the Coriolis parameter, with $f_0 = 9.3 \times 10^{-5}$ s^{-1}; $J(a, b)$ is the Jacobian of (a, b); τ is the wind stress acting at the upper surface and $\mathrm{curl}_z\tau$ is the vertical component of the wind stress curl; F_1, F_3, F_5 are the lateral frictional terms in the three layers. To express them the classical "constant eddy viscosity" hypothesis is assumed, with the shape:

$$F_i = -A\nabla^6\psi_i \qquad (2a)$$

the "biharmonic" friction needed to model enstrophy dissipation at high wavenumbers. Included in a simple linear form, B_5 is a bottom friction term:

$$B_5 = \epsilon\nabla^2\psi_5; \qquad (2b)$$

h_2, h_4 are downward perturbation displacements of the two interfaces from their equilibrium position:

$$\left.\begin{aligned} h_2 &= \frac{f_0}{g_2'}(\psi_1 - \psi_3) \\ h_4 &= \frac{f_0}{g_4'}(\psi_3 - \psi_5) \end{aligned}\right\} \tag{3}$$

where $g_2' = g\Delta\rho_2/\rho_0$ and $g_4' = g\Delta\rho_4/\rho_0$ are the "reduced" gravities at levels 2, 4. Here $g_2' = 0.03$ m s^{-2}; $g_4' = 0.013$ m s^{-2}. The streamfunctions ψ_2, ψ_4, responsible for advecting perturbation density at the interfaces, are evaluated as the weighted average of the streamfunctions in the adjacent layers:

$$\psi_2 = \frac{H_3\psi_1 + H_1\psi_3}{(H_1 + H_3)}; \quad \psi_4 = \frac{H_5\psi_3 + H_3\psi_5}{(H_3 + H_5)}.$$

We now define the concept of "density" tomography. Consider a tomographic section between a source S and a receiver R of acoustic pulses. The velocity component in the vertical plane along $S - R$ is u. The acoustic ray i shot from S to R has a travel time

$$T_i = \int_i \frac{ds}{C + u} = \int_i \frac{ds}{C_0 + \delta C + u} \approx \int_i \frac{ds}{C_0} - \int_i \frac{\delta C + u}{C_0^2}\, ds \approx \int_i \frac{ds}{C_0} - \int_i \frac{\delta C ds}{C_0^2}. \tag{4a}$$

The integral is along the acoustic path of ray i. The sound speed C in the instantaneous ocean realization is decomposed into an "unperturbed" sound speed $C_0(z)$, the climatological sound speed profile characteristic of the region, plus a perturbation δC. $C_0 \sim$ 1,500 m s^{-1}; for regions characterized by intense mesoscale activity, such as a section across the Gulf Stream, $\delta C \sim 30$ m s^{-1}; in the more quiescent part of the ocean, such as the Eastern Pacific, $\delta C \sim 10$ m s^{-1} is a reasonable estimate; here $\delta C/C_0 \sim 6 \times 10^{-3}$. An upper estimate of a current velocity, again in a relatively quiescent part of the ocean, can be $u \sim 10$ cm s^{-1} and $u/C_0 \sim 6 \times 10^{-5}$. Thus, in (4a) we use a Taylor expansion, retaining only the first two terms in the expansion, and we neglect $u/C_0^2 \ll \delta C/C_0^2$. $T_{i0} = \int_i (ds/C_0)$ is the "unperturbed" travel time, that is the travel time of acoustic ray i when traversing the unperturbed, climatological ocean defined by $C_0(z)$. T_{i0} can be directly evaluated tracing the acoustic rays through $C_0(z)$. Thus, the data used in the inverse are the differential travel times:

$$\delta T_i = T_i - T_{i0} \approx -\int_i \frac{\delta C}{C_0^2}\, ds. \tag{4b}$$

The data (4b) define "density" tomography: they are proportional to the sound-speed perturbation δC along the section, which is proportional to the temperature perturbation. If the considered region has a fairly stable temperature-salinity relationship, its average θ–S relation can be considered and a density perturbation measurement is obtained. Equation (4b) are the "perfect" data, with all possible sources of error temporarily neglected.

Consider now the pycnocline displacement from the mean $\zeta_i = -h_i$, with the h_i given by (3) in the model. Then:

$$\frac{\delta C}{C_0} = -\alpha \frac{N^2(z)}{g}\zeta_i$$

with

$$\alpha = \frac{\rho_0}{C_0}\frac{dC}{d\rho} \approx 25$$

(Munk and Wunsch, 1982) and $N^2(z)$ the local Brunt-Väisälä frequency. Also:

$$\frac{\delta C}{C_0} = \alpha^*\delta\theta + \beta\delta S = \alpha^*\delta\theta(1 + m\beta/\alpha^*)$$

with $\alpha^* \approx 3.19 \times 10^{-3}$ (°C)$^{-1}$, the thermal expansion coefficient for sound speed, and $m\beta/\alpha^* \approx 0.03$ (Munk and Wunsch, 1982). Then:

$$\delta\theta_i \approx \frac{1}{1.03\alpha^*}\frac{\delta C}{C_0} \simeq \frac{\alpha}{1.03\alpha^*}\frac{N^2(z)}{g}h_i$$

showing how the pycnocline displacement from the mean is proportional to the perturbation heat content at depth H_i.

Focus now on the average pycnocline displacement and the average pycnocline slope along the tomographic section. We can write the two model interfaces as

$$h_i = \bar{h}_i(t) + a_i(t)\left(x - \frac{L}{2}\right) + h_i'(x, y, t) \tag{5a}$$

where L is the length of the section and $i = 1, 2$.

$$\bar{h}_i(t) = \frac{1}{L}\int_0^L h_i(x, t)dx \tag{5b}$$

are the pycnocline spatial averages along L; $a_i(t)$ are the average slopes of the interfaces; $h_i'(x, y, t)$ are the interface fluctuations due to mesoscale activity.

The tomographic technique on ranges of the order of the gyre scale provides estimates of the average pycnocline displacement $\bar{h}_i(t)$, of the average pycnocline slope $a_i(t)$ and of their time evolution. These quantities will be the object of the simulations discussed in Section 3.

Two points here deserve discussion. First is the possibility of resolving the mesoscale activity, that is, of obtaining information about the term $h_i'(x, y, t)$ in Eq. (5a). The inverse procedure discussed in Section 3 capitalizes upon the specification of the field statistics, assigned as a covariance function for the sound speed perturbation δC. Good estimates of spatial averages and average pycnocline trends can be obtained using the covariance function appropriate for the longer scales of motion of the considered region.

Then, the mesoscale activity becomes a "noise" signal, added as a physical noise error to the data δT_i given by (4b). The mesoscale activity is thus filtered out. Moreover, the physical noise error due to smaller scale features, such as internal waves, increases with range. Over ranges as long as the gyre-scale, even when using covariance functions appropriate for the mesoscale, with correlation lengths of 100–200 km, it can be shown that the possibility of obtaining range-dependent information from the inversion is primarily a function of the assigned noise level (Malanotte-Rizzoli, 1984). For realistic oceanic noise values over ranges of ~2000 km, the basic quantities which can be measured are the spatial averages and mean trends. It must be emphasized, however, that the purpose of using tomography on the gyre-scale is exactly to obtain estimates of the above quantities, filtering out the mesoscale. That is why the forthcoming experiment will take place in the midlatitude Eastern Pacific Ocean, where the mesoscale energy peak is negligible compared to the energy levels in the long scales (Bernstein and White, 1977). That is also why the simulations of section 3 have been carried out in a relatively quiescent part of the model ocean. Had we chosen a tomographic section in a noisier and more frontlike region of the gyre, a 2000 km long tomographic section would provide almost no resolution of short-scale, sharp-gradient regions. Their main effect would be in increasing the noise level (Malanotte-Rizzoli, unpublished results).

The second point concerns the vertical resolution. The model is constituted by three layers. This is too poor a vertical resolution for a realistic tracing of acoustic rays. Thus, the vertical resolution in the simulated tomographic experiment is increased to 100 vertical layers, with a spacing of 50 m, through the interpolation procedure described in Appendix A. This is also the vertical resolution used in the inverse. In the actual experiment, the vertical resolution which can be achieved depends upon that of the hydrographic data from which the climatological sound speed profile $C_0(z)$ and the climatological vertical eigenmodes for the sound speed perturbation δC (used in the inverse) can be reconstructed. The data from which the profile $C_0(z)$ (shown in Fig. 5) was obtained had a vertical spacing of 20–50 m in the upper layer to 500 m depth; of 100 m from 500 to 1200 m and an increased spacing in the deeper layers, where $C_0(z)$ smoothly increases. An actual vertical resolution of 50–100 m is therefore possible. In the following simulations, the vertical profiles of the average displacement $\bar{h}(t, z)$ and of the average slope $a(t, z)$ are estimated with a vertical resolution of 50 m, thus providing the possibility of evaluating the vertical gradients of the pycnocline slopes (even though direct comparison of the slopes is shown only at the two model interfaces of 300 and 1000 m).

The above discussion bears upon the possibility of obtaining estimates of the mean velocity field from density tomography alone. The perturbation heat content along a tomographic section is proportional to the perturbation displacement as previously discussed. If a θ–S relationship is known for the region, the perturbation density field can be obtained. Through geostrophy, this density field will provide an estimate of the spatially averaged vertical shear of the geostrophic velocity component perpendicular to the section. The inversion procedure can be cast directly in terms of a velocity shear covariance function, thus giving estimates of the average vertical shear itself.

There is, however, an indirect way of evaluating the average absolute velocity field, for a tomographic array configuration with sections in both east–west (u) as well as north–south (v) directions. The results of the Section 3 will show that average pycnocline slopes along a section can be obtained very accurately by the inversion. As previously discussed, the vertical resolution of the estimated profiles allows us to evaluate the vertical gradients of the slopes. Tomography provides an instantaneous measurement of the slope. From the tomographic time series $a(t, z)$ the time average can be evaluated at every depth z over the duration of the proposed experiment (one year) or subintervals of it. Thus, a "climatological" vertical profile of the isopycnal slope would be obtained, which could be used in time-independent β-spiral calculations (Schött and Stommel, 1978). The time-averaged slopes would be moreover much less noisy than those inferred from subjective or polynomial fitting of point-wise hydrographic data taken at different times. Thus density tomography alone would provide an indirect measure of the absolute velocity field in the tomographic area.

3. The tomographic experiment in the model ocean: Heat content

The model used in the experiment simulation, Holland's quasi-geostrophic ERGCM, has been described in Section 2. The specific numerical experiment providing the model-ocean data set was carried out for the duration of 25 years. The interface ζ_2 at 300 m depth for the 20-year climatological mean (after spinup) is shown in Fig. 2. The x-axis is eastward; y northward; z upward. The ocean was forced by a surface wind stress with yearly and interannual fluctuations (5 years). The explicit expression used for the wind stress is

$$\left.\begin{aligned} \tau^{(x)} &= -a \quad \text{for} \quad y \geq y_0 + L \\ \tau^{(x)} &= a \cos\left[\frac{\pi(y - y_0)}{L}\right] \quad \text{for} \quad y_0 < y < y_0 + L \end{aligned}\right\} \tag{6}$$

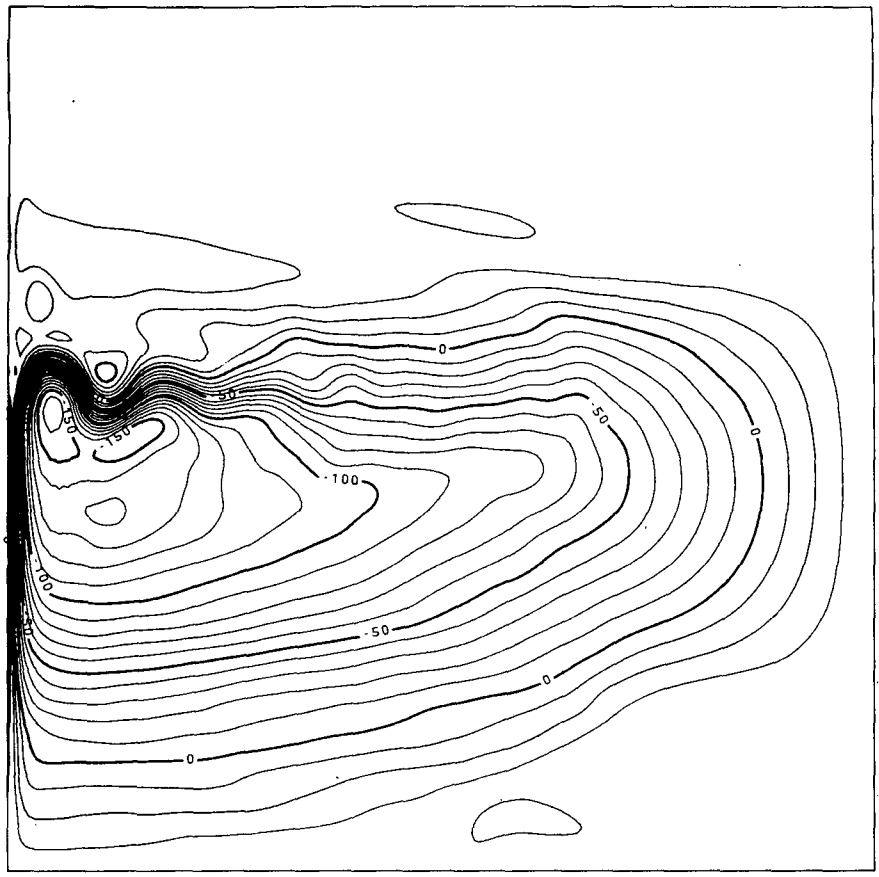

FIG. 2. Climatological mean (20-year average) of the interface ζ_2 at 300 m depth in m.

where the amplitude is

$$\left.\begin{aligned} a &= \tau_0[1 + a_1 \sin\omega_1 t + a_2 \sin\omega_2 t] \\ \tau^{(x)} &= a \quad \text{for} \quad y \leq y_0 \end{aligned}\right\};$$

$\tau^{(x)}$ is the x-component of the wind stress; the y-component is zero; y_0 = 800 km; L = 2,000 km; τ_0 = 1 dyn cm^{-2}; a_1 = 0.25; a_2 = 0.125; $\omega_1 = 2\pi/(360 \times 86{,}400)$ s^{-1}, the yearly frequency; $\omega_2 = 2\pi/(5 \times 360 \times 86\,400)$ s^{-1}, the 5-year frequency. The time evolution of the wind stress amplitude is shown in Fig. 3 (time in days from the beginning of the experiment). The yearly and interannual fluctuation of the surface forcing function insure fluctuations of average properties, like heat content, in the various oceanic regions. Mesoscale eddy activity, due to instabilities in the Gulf Stream region, are superimposed upon this directly induced transience.

The individual "snapshots" of the model-ocean data set are 8-days averages of successive realizations, which allows the resolution of the mesoscale energy peak without an excessive number of data sets.

Figure 4 shows the pattern of the first interface, with $\zeta_2 = -h_2$, with h_2 given by (3), at 300 m depth, for day 3606, the initial day of the simulated tomography experiment. Two gyre-scale regions appear with different mesoscale properties. A "southern" ocean (dotted box in Fig. 4) embodying the region south of the western boundary jet, characterized by intense mesoscale activity. The eddy activity is not only important immediately south of the meandering jet but also in the southernmost region, due to processes of baroclinic instability of the return Sverdrup flow. In contrast, the "eastern" ocean (continuous box in Fig. 4) is relatively quiescent, more analogous to what presumably are conditions in the Eastern Pacific, in the Sverdrup recirculation region of the subtropical gyre. Section AB, 2400 km long in the eastern ocean (Fig. 4) was chosen to carry out the majority of the tomography experiments as representative of the Eastern Pacific. The successive phases of the density tomography experiment will now be described.

a. Reconstruction of the sound speed perturbation field

The relationship of the sound speed perturbation to the pycnocline displacement from the mean at various depths is:

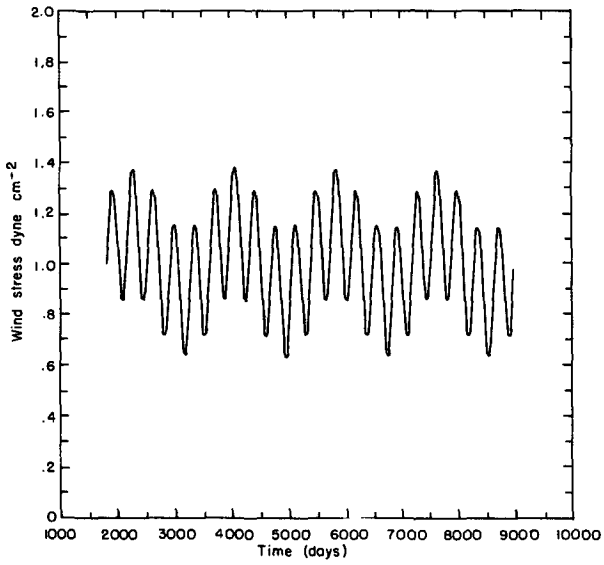

FIG. 3. Time evolution of the wind stress amplitude. Horizontal coordinate: time in days. Vertical coordinate: dyn cm^{-2}.

$$\frac{\delta C_p}{C_{0p}} = \frac{1}{C_{0p}} \frac{dC_p}{d\rho} \frac{d\rho}{dz} \zeta(x, z) = -\frac{\alpha N^2(z)}{g} \zeta(x, z) \quad (7a)$$

where the subscripts p indicates potential quantities, g is the gravity acceleration, 9.8 m s^{-2}; $N^2(z)$ the Brunt-Väisälä frequency and

$$\alpha = \frac{\rho_0}{C_{0p}} \frac{dC_p}{d\rho} \sim 25$$

(Munk and Wunsch, 1982).

From quasi-geostrophy (Flierl, 1978)

$$\zeta = -\frac{f_0}{N^2(z)} \psi_z, \quad (7b)$$

$$\frac{\delta C_p}{C_{0p}} = \frac{\alpha f_0}{g} \psi_z \quad (7c)$$

which relates the perturbation δC_p of the sound speed field to the quasi-geostrophic streamfunction. From (7c) it is evident that "density" tomography, providing a measure of δC_p, does not "see" the barotropic

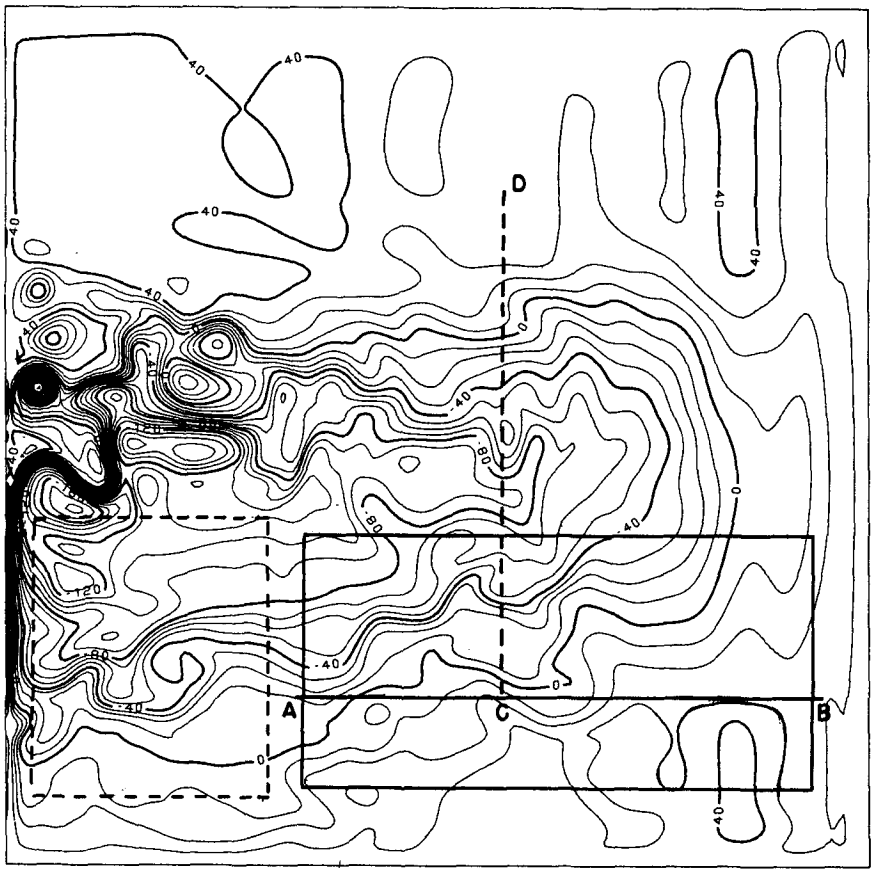

FIG. 4. Pattern of the interface ζ_2 at 300 m depth for day 3606 of the numerical experiment. Dotted box: "Southern" ocean. Continuous box: "Eastern" ocean. AB and CD are the tomographic sections.

mode. The relationship between the pycnocline deviation from the mean in the continuously stratified ocean and the layered representation is also clear. In the layered representation:

$$\zeta_n = -\frac{f_0}{g/\rho_0(\rho_{n+1} - \rho_{n-1})}(\psi_{n-1} - \psi_{n+1})$$

$$= -\frac{f_0}{g'_n}(\psi_{n-1} - \psi_{n+1}) = -h_n \quad \text{with} \quad n = 2, 4.$$

Three vertical layers give a vertical resolution that is too poor for the "direct" problem, that is for tracing the acoustic rays from a given source to a given receiver. A realistic tracing of acoustic rays requires a vertical resolution approximating as well as possible a continuous stratification. Appendix A describes the interpolation procedure used to obtain a vertical resolution capable of approximating the continuous representation given by (7a, b, c).

The inversion procedure is cast in terms of linear predictors for the vertical structure of the perturbation δC_p. The proper set of linear predictors, consistent with the model used, are the quasi-geostrophic dynamical eigenmodes of $\delta C_p/C_{0p}$, that is the eigenmodes of the pycnocline displacement ζ, as clear from (7b, c). Again from (7b, c), the latter ones are given by the vertical shear of the dynamical eigenmodes for the streamfunction ψ, solution of the Sturm-Liouville problem:

$$\frac{d}{dz}\left[\frac{f_0^2}{N^2(z)}\frac{dF_n}{dz}\right] = -\lambda_n^2 F_n,$$

$$F_{nz} = 0 \quad \text{at} \quad z = 0, -H \qquad (8)$$

where $\lambda_n^2 = 1/R_n^2$, the eigenvalue, is the reciprocal of the associated baroclinic Rossby radius. The three layer model allows for one barotropic and two baroclinic modes. Only the last two are obviously necessary in a density tomography experiment. From the "box" representation of the dynamical eigenmodes we pass to a "continuous" representation through the interpolation procedure described in Appendix A, obtaining a vertical resolution of 100 layers over 5000 m depth with 50 m vertical spacing. Also, the required eigenmodes must be representative of the average, or climatological, conditions for the considered area. Thus, they are evaluated from the climatological 20 year mean of Fig. 2, in the eastern part of the gyre (continuous box of Fig. 4). From the two baroclinic eigenmodes for the streamfunction $\bar{\psi}$, the climatological eigenmodes $\overline{\delta C_1}/C_{0p}$ and $\overline{\delta C_2}/C_{0p}$ are obtained through (7c) where the bar refers to quantities evaluated in the climatological mean.

The eigenmodes $\overline{\delta C_1}$ and $\overline{\delta C_2}$ themselves can be evaluated specifying a basic reference profile $C_0(z)$. As evident from (7b, c) the streamfunction ψ is related to the perturbation quantities. A reference profile $C_0(z)$ might have been obtained from the model itself, using the three layers constant reference densities ρ_1, ρ_3, ρ_5, with the assumption of a linear equation of state and interpolating in the vertical. Such a profile, however, would be the same all over the model ocean, identical in regions with very different mesoscale properties, like the quiescent Eastern part and the active region south of the Gulf Stream. The actual average sound speed profile characteristic of the Eastern Pacific is rather different from the one typical of the Sargasso Sea. Thus, for a more realistic simulation of the tomographic experiment, an Eastern Pacific average profile was used for $C_0(z)$ (courtesy of J. Spiesberger). This is shown in Fig. 5. It must be pointed out, however, that the specification of a different $C_0(z)$ would not affect at all the results of the inverse and of the simulations. The quantities which the model fully provides are the perturbation quantities, as shown by (7a, b, c). The estimate of the inverse is the difference between a perturbed state, provided by the model through (7c), and an average reference field C_0 which can be chosen practically arbitrarily. Any change in the choice of $C_0(z)$ does not affect the model properties which determine only the ratio $\delta C_p/C_{0p}$. The climatological eigenmodes $\overline{\delta C_1}$, $\overline{\delta C_2}$, evaluated using the $C_0(z)$ of Fig. 5, are shown in Fig. 6.

Equation (7c) itself provides the ratio $\delta C_p/C_{0p}$ through vertical interpolation of the streamfunction field ψ. Using the basic reference profile $C_0(z)$ of Fig. 5, the total, perturbed sound speed field of each realization is then given by

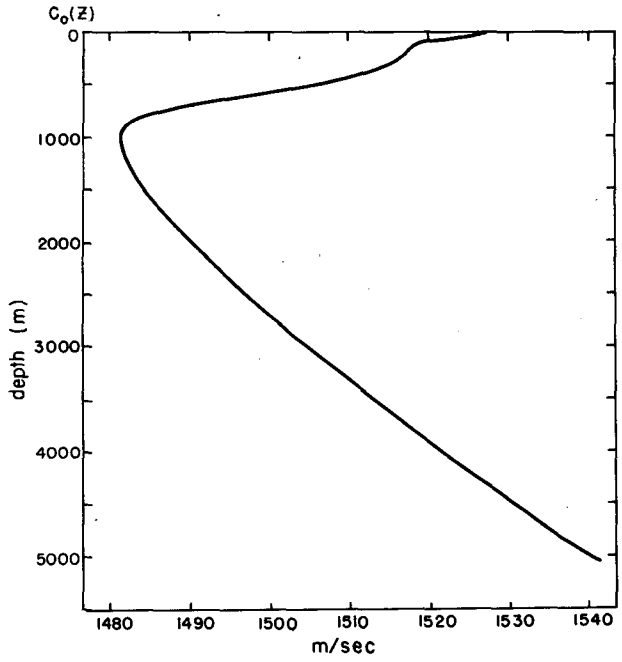

FIG. 5. Average sound speed profile for the Eastern Pacific (courtesy of J. Spiesberger).

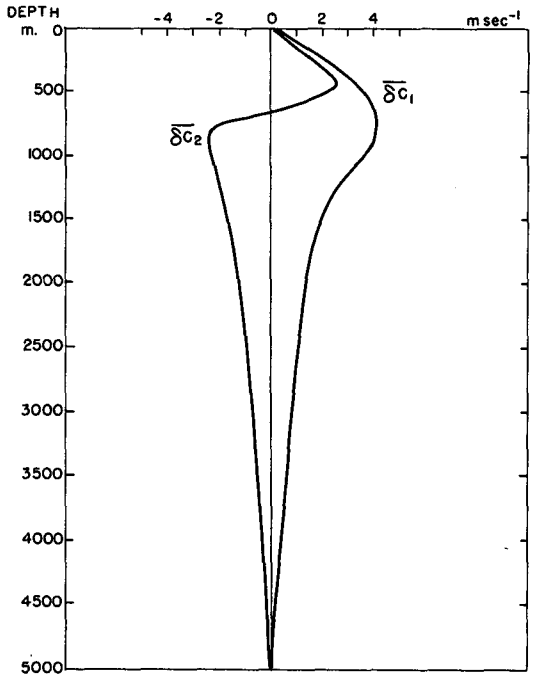

FIG. 6. The first, $\overline{\delta C_1}$, and second, $\overline{\delta C_2}$, baroclinic vertical eigenmodes for the sound speed perturbation field as reconstructed from the climatological mean in the "Eastern" ocean box of Fig. 6.

$$C_p(\mathbf{x}) = C_{0p}(z) + \delta C_p(\mathbf{x})$$

$$= C_{0p}(z) + C_{0p}(z)\cdot\left(\frac{\alpha f_0}{g}\right)\psi_z(\mathbf{x}). \qquad (9)$$

To evaluate the perturbation heat content $\delta\theta$ we use the linear relationship

$$\frac{\delta C_p}{C_{0p}} = \alpha^*\delta\theta + \beta\delta S = \alpha^*\delta\theta\left(1 + \frac{m\beta}{\alpha^*}\right) \qquad (10)$$

which relates $\delta\theta$ to δC_p. $\alpha^* = 3.19 \times 10^{-3}$ (°C)$^{-1}$ and $m\beta/\alpha^* \simeq 0.03$ (Munk and Wunsch, 1982). Thus

$$\delta\theta = \frac{1}{1.03\alpha^*}\frac{\delta C_p}{C_{0p}}. \qquad (11)$$

The vertical slice of $\delta\theta$ in C° over section AB is shown in Fig. 7 for day 3606, the initial day of the experiment. The negative maximum of −0.4°C is in the eastern part corresponding to a negative maximum in δC of −2 m s^{-1} with local cold eddies of −0.25 and −0.1°C in the interior of the section. Section AB has been chosen for the modeling simulations for its similarity in isopycnal trends to the hydrographic Pacific section at 35°N, the properties of which were recently discussed by Kenyon (1983).

Figure 8a is from Kenyon's paper, showing the vertical section of in situ temperature in °C. As a comparison, Fig. 8b shows the model interface at 300 m depth, with the isopycnal displacement slightly negative at A and a positive slope in eastward direction. This eastward trend characterizes sections AB and is analogous to the isotherm slopes of Kenyon's section in the region enclosed between vertical lines in Fig. 8a, located in the Eastern Pacific.

To make a crude comparison with the heat content values of the model, a "perturbation" heat content for Kenyon's section was evaluated according to

$$\delta T(z) = T(z) - \bar{T}(z)$$

where $T(z)$ is the in situ temperature value at each depth z and $\bar{T}(z)$ is the average temperature value at depth z for the Eastern part defined in Fig. (8a). The $\delta T(z)$ data showed similarity to the perturbation heat pattern of Fig. 7 between stations 7 and 20 and in the vertical layer from 200 to 700 m depth. In fact, $\delta T(z)$ values were positive or slightly negative at the western stations, becoming increasingly negative on the eastern side. The total length of the section

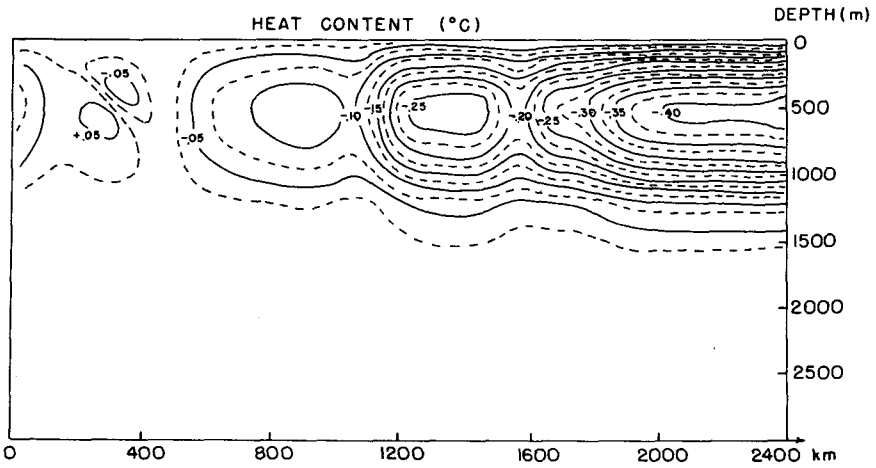

FIG. 7. Vertical slice for the perturbation heat content $\delta\theta$ in °C for section AB at day 3606.

between stations 7 and 20 is 2560 km, comparable to the model section of 2400 km. An illustrative comparison can be made between the spatial averages $\overline{\delta T}(z)$ at each level z evaluated from Kenyon's section and the corresponding average values in the model ocean. Table 1 shows such a comparison:

TABLE 1. Comparison between $\overline{\delta T}(z)$ for Kenyon section and model area.

Depth (m)	Hydrographic section (°C)	Model ocean (°C)
200	−0.152	−0.112
250	−0.185	−0.134
300	−0.234	−0.153
400	−0.298	−0.178
500	−0.271	−0.188
600	−0.147	−0.187
700	−0.068	−0.177

The average perturbation heat contents are of the same order of magnitude. Obviously, this is a very crude comparison. It assures us, however, that our model ocean is sufficiently realistic in that values of the same order of magnitude as those observed are found.

Another quantity—equivalent to the perturbation heat content—can be directly compared between the model ocean and the results of the tomographic simulation, that is the pycnocline displacement itself. From (7a) and (11) in fact:

$$\zeta = \frac{-g}{\alpha N^2(z)} \frac{\delta C_p}{C_{0p}} = \frac{-1.03 g \alpha^*}{\alpha N^2(z)} \delta\Theta \tag{12}$$

and particularly the spatial average $\bar{\zeta}(z)$ at each depth, equivalent to the average perturbation heat content. The model provides the two natural levels where to make the comparison, 300 and 1000 m, where interfaces are defined in the layered version. From (12) it is clear that $\zeta(x, z)$ is the "mirror image" of $\delta\theta(x, z)$.

b. *The direct and inverse problems*

The basic steps of the inversion procedure are now summarized.

The data measured in the tomographic experiment are the travel times of different acoustic rays reaching the receiver. The measured travel times are referred to the reference travel times, that is the travel times of the rays in the reference, unperturbed ocean defined by $C_0(z)$. For each ray the reference travel times are thus defined by

$$T_{i0} = \int_{\Gamma_{i0}} \frac{ds}{C_0(z)} \tag{13}$$

where Γ_{i0} is the unperturbed ray path i in $C_0(z)$. In the model ocean an acoustic source was located at A and a receiver at B, along the AB section of Fig. 4. Both were at 1000 m depth, the minimum of $C_0(z)$ (Fig. 5).

The rays through the instantaneous, perturbed realizations have travel times:

$$(T_i)_{\text{perturbed}} = \int_{\Gamma_i} \frac{ds}{C(x, z)} \tag{14}$$

where Γ_i are the perturbed ray paths. The data of the experiment are the differential travel times δT_i:

$$\delta T_i = ((T_i)_{\text{perturbed}} - T_{i0}) + \epsilon_i. \tag{15}$$

The appropriate $(T_i)_{\text{perturbed}}$ are the travel times of the matching acoustic rays identified according to the number of turning points, and ϵ_i is a noise signal, embodying all possible instrumental errors as well as physical noise due to smaller scale processes like internal waves. The δT_i are the data we would measure in the actual experiment. We call (15) the "nonlinear direct problem."

The perturbed profile and perturbed paths can be related to the reference ocean by

$$\left.\begin{aligned} C(x, z) &= C_0(z) + \delta C(x, z) \\ \Gamma_i &= \Gamma_{i0} + \delta\Gamma_i \end{aligned}\right\}$$

where $\delta\Gamma_i$ is the displacement of the perturbed ray path from the unperturbed one.

The inversion procedure is based upon the double assumption (i) $\delta C/C_0 \ll 1$; (ii) $\delta\Gamma_i/\Gamma_{i0} \ll 1$. Then one can use a Taylor expansion of (14) around the reference states $C_0(z)$; Γ_{i0} and retain only the first terms in the expansion. This linearization leads to the approximate expression for the differential travel times given by

$$\delta T_{i0} \approx -\int_{\Gamma_{i0}} \frac{\delta C(x, z) ds}{C_0^2(z)} + \epsilon_i. \tag{16}$$

In (16) $\delta C(x, z)$ is evaluated in the perturbed section along the reference ray paths Γ_{i0}. We call (16) the "linearized direct problem." The tomographic experiment has been carried out using as data both (15) and (16) for comparison experiments. Obviously, the possibility of using (16) as data exists only in the model ocean, where the instantaneous perturbed field is known. In the true experiment, only the δT_i given by (15) are known.

The inverse problems in tomography consists in using the differential travel times (15) along N paths (and any other data) to obtain an estimate of $\delta C(\mathbf{x})$ of the perturbation field. The procedure used here is the stochastic inverse developed by Cornuelle (Cornuelle, 1983; Cornuelle *et al.*, 1984). The details of the inverse are given in Appendix B.

The stochastic inverse bears upon the specification of the field statistics which is given through the expected covariance function for the sound speed perturbation:

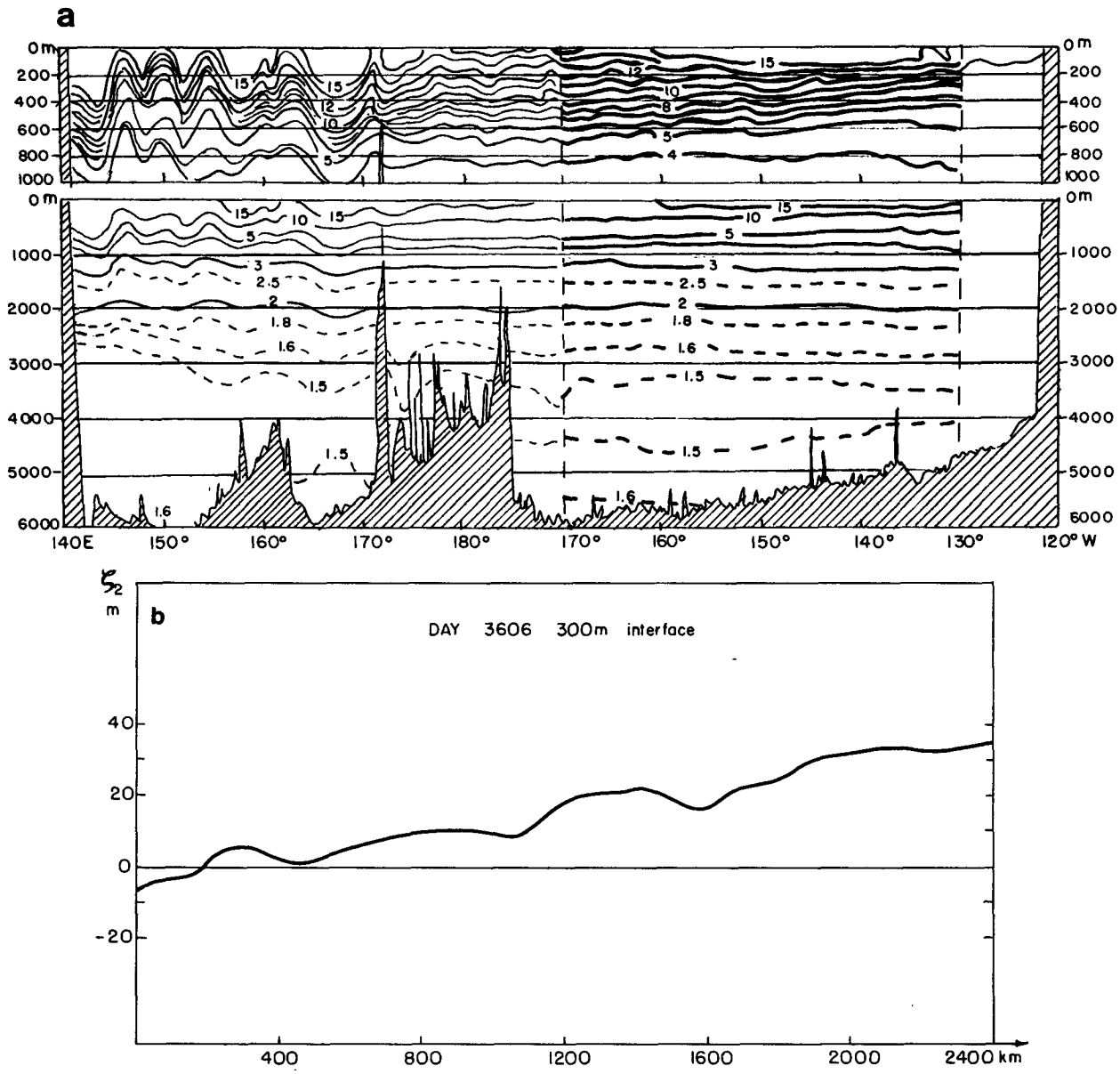

FIG. 8. (a) Isotherms (°C) along a hydrographic section across the Pacific Ocean at 35°N (from Kenyon, 1983). (b) Model interface (m) at 300 m depth at day 3606.

$$G(\mathbf{x}_1, \mathbf{x}_2) = \langle \delta C(\mathbf{x}_1) \delta C(\mathbf{x}_2) \rangle. \quad (17)$$

Following Cornuelle (1983) (17) is specified as

$$\langle \delta C(\mathbf{x}_1) \delta C(\mathbf{x}_2) \rangle = \sum_{j=1}^{2} \beta_j H[(x_2 - x_1)^2 + (y_2 - y_1)^2] F_j(z_1) F_j(z_2). \quad (18)$$

The covariance is thus expanded into the set of sound speed perturbation eigenmodes $F_j(z) = \overline{\delta C_j(z)}$ reconstructed from the climatological mean (Fig. 6); $H[(x_2 - x_1)^2 + (y_2 - y_1)^2]$ is the horizontal covariance function assumed to be homogeneous and isotropic. The eigenmodes as well as the horizontal covariance are normalized. Then, the β_j, the weights to be assigned to the modes in the inversion, are the expected variances of the two dynamical modes in the perturbed realizations from the climatological mean (Cornuelle, 1983). The β_j set the overall energy level to be expected for each mode j. They were evaluated at each point x along section AB for different perturbed realizations and showed little variability as section AB evolves very smoothly. Thus, ensemble-average values were constructed;

$$\beta_1 = 0.6 \text{ (m s}^{-1})^2; \quad \beta_2 = 0.2 \text{ (m s}^{-1})^2. \quad (19)$$

These values were consistently used in the inversions carried out for section AB.

For the horizontal part of the covariance function, examination of the tomographic section AB during the full year 10 revealed a mesoscale energy peak much smaller than that typical of a region with intense mesoscale activity. This feature of the model is also characteristic of the Eastern Pacific subtropical gyre. A spectral analysis of hydrographic and XBT data from several sources shows a striking order-of-magnitude decrease in the distribution of baroclinic mesoscale eddy energy occurring abruptly east of the 170°W meridian in the midlatitude North Pacific (Bernstein and White, 1977). The northeast Pacific thus appears to be nearly void for mesoscale eddies. This is also evident simply looking at the map of isotherms of the Kenyon's Pacific section (Fig. 8a).

Covariance functions in the model were evaluated from the isotropic energy spectra computed for the Eastern box of Fig. 4 for different realizations. They showed the first zero-crossings in the range 400–600 km, consistent with the examination of the model interfaces which indicated rather long correlation lengths. Thus, the simplest choice was made for the horizontal covariance, that is a Gaussian, homogeneous and isotropic, with the width of 500 km:

$$H[|\mathbf{x}_2 - \mathbf{x}_1|] = \exp\{-|\mathbf{x}_2 - \mathbf{x}_1|^2/(500\text{ km})^2\}. \quad (20)$$

(20) was used in the time-evolution simulation experiment (Section 3c).

In all the inversions that follow a set of 6 basic eigenrays was used. Increasing the number of reference eigenrays did not improve significantly the estimate of the average perturbation field (Malanotte-Rizzoli, 1984).

c. *Time evolution*

The most important feature of tomography in a gyre-scale experiment is that it offers the possibility of measuring the time evolution of average quantities.

In the present experiment the estimated quantity is the perturbation heat content, or pycnocline displacement, at various depths, averaged over section AB. The pycnocline displacement was shown in Fig. 8b. This trend is typical of section AB. Isopycnal displacements are slightly negative at A, with a marked slope in eastward direction. The average pycnocline displacements at 300 and 1000 m depth evolved smoothly during all year 10. Values for $\bar{\zeta}_2$ ranged from an initial value of 15.83 m at day 3606, to a maximum of 20.41 m at day 3798, to the minimum of 14.79 m on the final day 3958. Values of $\bar{\zeta}_4$ ranged from the initial value of 8.13 m at day 3606, to maxima of 13.43 m at day 3734 and 13.54 m at day 3894, to the final value of 10.26 m at day 3958. For a vertical temperature gradient of $d\theta/dz = 0.02$°C m^{-1} in the thermocline region, corresponding to the 1000 m interface, this average displacement of ~10 m gives an average rms amplitude $|\delta\theta| = 0.2$°C, in agreement with the model perturbation heat content at that level.

The tomographic experiment was carried out for the whole year 10 at 16 days interval using the linearized direct problem (16). Every third of these inversions, a "true" inversion was carried out using the nonlinear direct problem (15), that is the data we would measure in the real experiment.

Figure 9 shows the result of the "true" inversion for the initial day 3606. The vertical profile of the perturbation heat content $\delta\theta$ in °C is shown for each 50 m depth, averaged over Section AB, to the depth of 3000 m. The continuous, thick line is the model heat content. The thin line is the result of the inversion with relative error bars. The error bars are evaluated directly in the inversion as discussed in Appendix B. Typical values are of ~0.06–0.08°C for an average perturbation heat content of ~0.25°C. The shaded part indicates the surface layer not sampled by the acoustic rays. The result of the inversion is that the ocean seems slightly "too cold" compared to what it actually is. Table 2 gives the values of the perturbation heat content integrated over different vertical layers respectively from the model, from the inversion using (15) (Inversion 1) and from the inversion using (16) (Inversion 2). In contrast to the "true" inversion, the inversion using the δT_i given by (16) consistently underestimates the perturbation heat content.

Focussing on time variability, Figs. 10a and b show the evolution during year 10 of the perturbation heat content at (a) 300 m depth and (b) 1000 m depth, corresponding to the two model interfaces. Heat content values are in (negative) °C. The pycnocline displacement is the "mirror image" of the perturbation heat content. The evolution of the perturbation heat content from the model always lies between the inversion result using (16) (underestimate) and the inversion result using (15) (the ocean seems too cold).

Concentrating only on the "true" inversion, at 300 m depth, the perturbation heat content from the inversion is "off" from the model in the range from a minimum of −10.5% at day 3606 to a maximum of −18% at day 3894, with an average of −15.6% (the minus sign indicates that the ocean seems too cold). At 1000 m depth, the percentage error lies in the range from a minimum of −14.3% at day 3942 to a maximum of −17.6% at day 3702 with an average value of −16.6%. The estimate is slightly better for the 300 m interface. Over one year of time evolution, the inversion gives an estimate of the average heat content having an average cold bias of approximately −0.025°C relative to the model average value of −0.159°C at 300 m depth; and an average cold bias of approximately −0.035°C relative to the model average value of −0.210°C at 1000 m. These

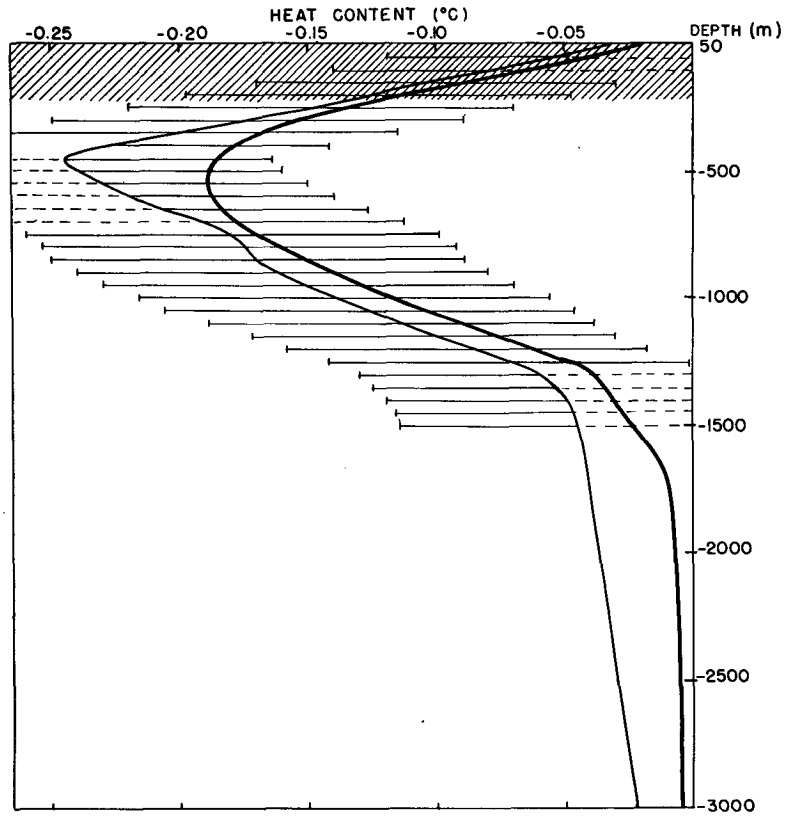

FIG. 9. Heat content profile averaged over section AB at day 3606 from the model (continuous thick line) and from the inversion (continuous thin line). Thin horizontal lines: error bars. The shaded surface region is not sampled by the acoustic rays.

biases, even though significant, are not dramatic. They are due to the linearization assumption upon which the inverse capitalizes using the linearized expression for the travel time data given by (16) (see Appendix B).

The fact that the biases in the heat content estimates are not extremely large does not depend on the simple vertical structure of section AB and on its smooth time evolution. Sections with a much more complex vertical structure and a much more enhanced mesoscale energy peak have been considered (like section CD discussed in Section 3e which crosses the subtropical gyre). The cold (or warm) biases resulting from the first inversion increase nonlinearly with increasing average heat content $\delta\theta$, but their magnitude does not depend upon the details of the structure of the section.

TABLE 2. Perturbation heat content.

Layers (m)	Model	Inversion 1	Inversion 2
0–300	−0.091	−0.093	−0.064
300–1000	−0.166	−0.197	−0.136
1000–2000	−0.030	−0.069	−0.026
2000–3000	−0.0053	−0.029	−0.0016
3000–4000	−0.0014	−0.020	−0.0008

The most important feature of tomography for the time evolution of properties is that the measurements are synoptic over large areas. The evolutions of Figs. 10a and b provide a time series of the instantaneous, average heat contents along section AB at different depths. Figures 10a and b show these time evolutions only at the depths of 300 and 1000 m, but it must be born in mind that the vertical resolution provided by the inverse is of 50 m. Thus the time evolution of the average pycnocline displacement can be monitored with great resolution throughout the depth of the oceanic layer sampled by the acoustic rays. In the present simulations, this excludes only a surface layer $\sim$ 150 m thick. Thus, an estimate can be obtained of the frequency spectrum of the average pycnocline displacement in layers below the surface mixed layer, in which the circulation is basically wind-driven. It is obvious that in this subsurface layer the frequency spectrum of the pycnocline displacement is correlated with the frequency spectrum of the surface forcing function, the wind stress. In fact, evaluation of the energy spectra of the two model interfaces over year

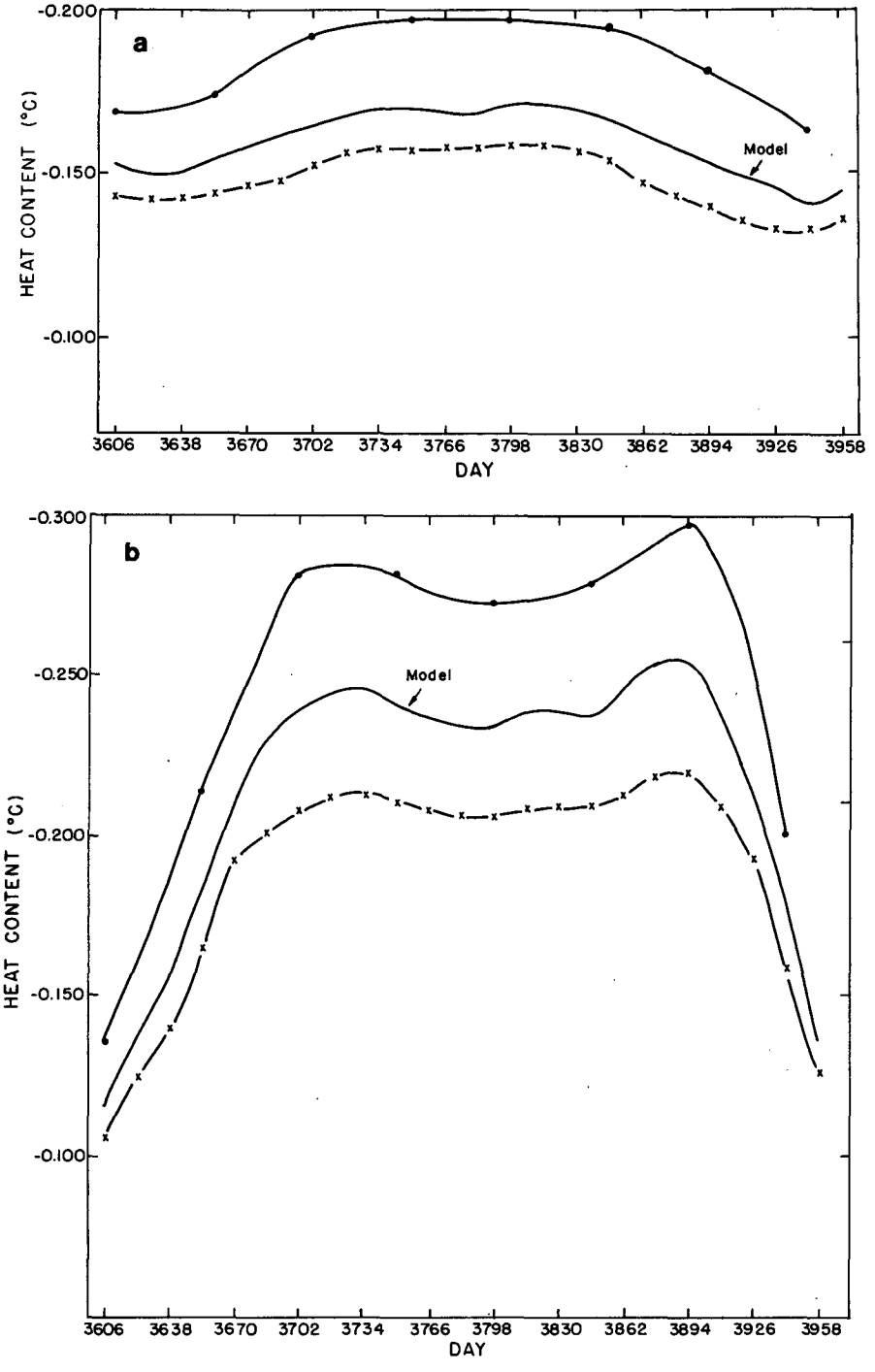

FIG. 10. (a) Evolution during year 10 of the perturbation heat content at 300 m depth. Model: continuous line. Inversion using the δT_i defined by (15): continuous-dotted line. Inversion using the δT_i defined by (16): broken-cross line. (b) As in (a) but for the perturbation heat content at 1000 m depth.

10 gave 57% of the total energy concentrated at the yearly frequency of the wind stress $\omega_1 = 0.2 \times 10^{-6}$ rad s^{-1}; 32% in the mean and smaller values at higher harmonics. This suggests the important possibility of inferring the frequency spectrum of the surface forcing function—the wind stress—from the frequency spectrum of the average pycnocline displacement, in the subsurface layer of direct wind driving.

d. Iteration

The results of Section 3c show that the inversion, as it was designed for the 1981 mesoscale experiment and as it has been used in these modeling simulations, needs to be improved when going to gyre-scale ranges, one order of magnitude bigger. The simplest way to eliminate the biases in average heat content estimates which result from the first inversion is the approach of iteration, in which the "frozen" rays assumption is relaxed and successive approximations to the perturbed ocean are constructed.

The data obtained from the real experiment are the travel times measured in the instantaneous realization $(T_i)_{\text{perturbed}}$ given by (14). The reference travel times are those of the matching eigenrays traced through the reference profile $C_0(z)$. These unperturbed ray paths Γ_{i0} and the differential travel times δT_i given by (15) are used to carry out the first inversion, which provides a first estimate of the perturbation sound speed field $\delta\hat{C}_1(x, z)$. This estimate is used to construct a "new" reference ocean:

$$C_1(x, z) = C_0(z) + \delta\hat{C}_1(x, z). \tag{21a}$$

The acoustic rays are then traced through $C_1(x, z)$ and, through the usual matching process, they will provide new reference travel times:

$$(T_{i0})_1 = \int_{(\Gamma_{i0})_1} \frac{ds}{C_1(x, z)} \tag{21b}$$

where $(\Gamma_{i0})_1$ are the new ray paths through $C_1(x, z)$. The new differential travel times are

$$(\delta T_i)_1 = (T_i)_{\text{perturbed}} - (T_{i0})_1. \tag{21c}$$

The successive inversion uses the $(\delta T_i)_1$ as data and the new ray paths $(\Gamma_{i0})_1$. This provides a second estimate $\delta\hat{C}_2(x, z)$ and a successive approximation to the instantaneous, perturbed realization:

$$C_2(x, z) = C_1(x, z) + \delta\hat{C}_2(x, z). \tag{21d}$$

Again the rays are traced through $C_2(x, z)$ obtaining new reference travel times $(T_{i0})_2$ and new paths $(\Gamma_{i0})_2$, used in the successive inversion, and so forth. The iteration is stopped when a percentage error e_i between the new travel times $(T_{i0})_n$ and the data $(T_i)_{\text{perturbed}}$ is below 0.01%. The iteration has been carried out for section AB during day 3606.

Figure 11 shows the average heat content vertical profile of section AB from the model; from the first inversion (Inversion a) and after the fourth iteration (x-profile). The iteration might actually have been stopped after the third iteration. In the x-profile of Fig. 11, result of the iteration, the maximum errors are of −0.02°C with respect to the true value of −0.19°C in the surface layer above 500 m depth; of +0.025°C with respect to −0.18°C in the layer between 500 and 1500 m; and of 0.0015°C with respect to 0.01°C in the deep layer. The maximum percentage error all over the water column is ~10–15%. The two successive oceans $C_3(x, z)$ and $C_4(x, z) = C_3 + \delta\hat{C}_4$ are both accurate approximations to the true ocean. Table 3 gives the heat contents averaged over different vertical layers from the model; from the first inversion and after the iteration process. The average heat content profile after the iteration process (x-points in Fig. 11) is indeed a good estimate of the model profile, as well as the heat content values of Table 3.

e. The warm section CD

The tomographic simulations discussed in the previous chapters were all carried out on the zonal section AB of Fig. 4. Section AB is however weakly perturbed.

One might conjecture whether the previous results, in particular the good estimates obtained through the iteration, hold because of the weakness of the perturbation field. Thus, a more perturbed section was considered. The chosen section, marked as CD in Fig. 4, is very different from AB. Section CD, again 2400 km long, is a meridional section in the eastern part of the model ocean. It crosses the subtropical gyre and the pycnocline displacement at 300 m depth has consequently a concave trough shape, going from slightly positive values at the southern boundary C (+12.24 m) to a large, negative displacement roughly in the center (−92.5 m) and successively rising to positive values at the northern extremity D (+35.5 m). The second interface, instead, at 1000 m depth exhibits only mesoscale activity.

Section CD is rather warm. The main feature of the section is the core of the subtropical gyre, with the maximum sound speed perturbation value of $\delta C \sim +9$ m/sec at 300 m. Further, smaller eddies are also present in the interior, including a negative one at the northern extremity, with a maximum value $\delta C \approx -3$ m/sec. The pattern of the heat content anomaly in the CD vertical slice is shown in Fig. 12. The interior shape of the subtropical gyre is evident, with a maximum perturbation value $\delta\theta \approx 1.8$°C. For a vertical temperature gradient of $d\theta/dz \approx 0.02$°C/m in the thermocline region, now corresponding to the 300 m interface, a maximum displacement of ~100 m gives a maximum amplitude $|\delta\theta| = 2$°C, which is what is observed in the section. Thus, section CD constitutes an example of rather perturbed conditions.

The two model interfaces in CD (not shown) at 300 m, 1000 m depth are very different from section AB. The 300 m interface follows the concave trough shape of the gyre interior while at 1000 m depth a succession of less intense, and mostly warm mesoscale eddies is found. Thus, the mesoscale energy peak along CD is much more pronounced.

As CD protrudes much more northward than the "Eastern Ocean" box of Fig. 4, an analogous "Eastern

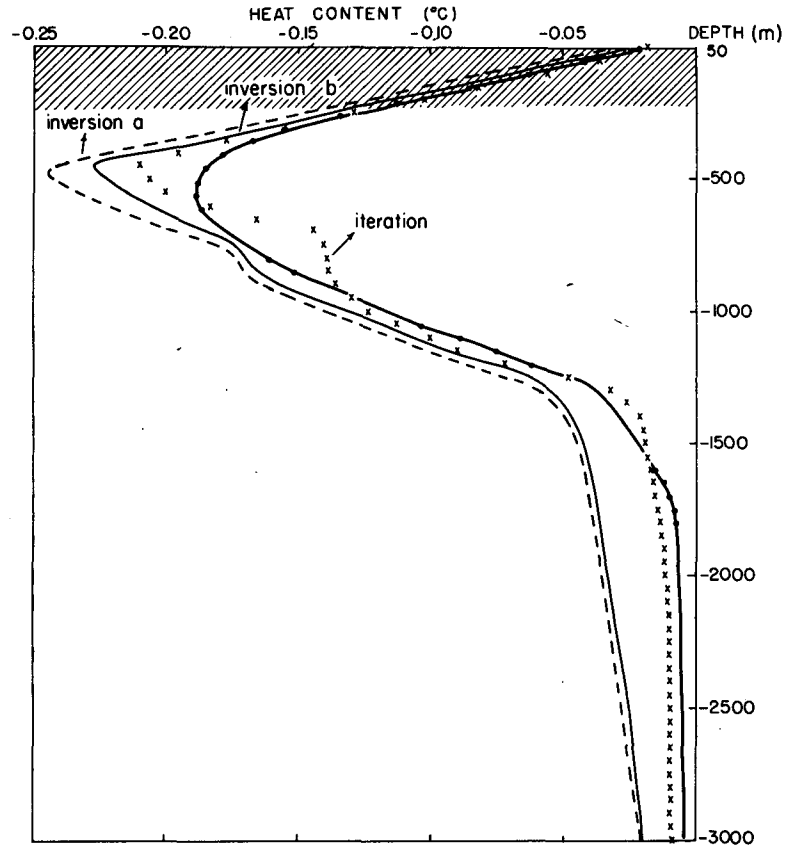

FIG. 11. Average heat content vertical profile for section AB at day 3606 from the model (continuous thick line); from the first inversion, inversion a (broken line); after the iteration (cross symbols). Inversion b: inversion carried out with the covariance function including a spatial mean. The shaded surface layer is not sampled by the acoustic rays.

Ocean" meridional box was considered, centered around CD, to reconstruct the climatological baroclinic eigenmodes $\overline{\delta C_1}$ and $\overline{\delta C_2}$ from the 20-year mean. The two modes thus obtained (not shown) have a shape very similar to the previous modes used for section AB and shown in Fig. 6. Their maxima are however located at different—and smaller—depths consistent with the fact that the most perturbed layer is between 250 and 700 m.

Covariance functions for the sound speed perturbation field δC evaluated along section CD had the first zero-crossing at ~500 km for the 300 m interface but only at ~150 km for the 1000 m interface. The isotropic energy spectra for the δC field evaluated at the 300 and 1000 m interfaces in the "Eastern" ocean of Fig. 4 showed that energy was concentrated at the longer wavelengths. Also, the direct evaluation of the variance in the mean perturbation $\overline{\delta C}^2$ and in the eddy field $\langle|\delta C - \overline{\delta C}|^2\rangle$ for different realizations gave in the eastern ocean variances in the mean comparable to the eddy variance. The specification of the field statistics can be improved by including the variance in the mean into the covariance function given by (18). This improves the initial estimate $\delta\hat{C}_1$ given by the inverse and the iteration process requires a smaller number of iterations (Malanotte-Rizzoli, 1984). Thus, evaluation of the variance in the mean for each baroclinic mode $F_j = \overline{\delta C_j(z)}$ gives the estimate of the energy level in the spatial mean. This mean value is added to the mode covariance $H(r)$.

The inclusion of the spatial mean into the covariance function can improve significantly the results of the first inversion. This is shown in the vertical profile of the average heat content for section AB shown in Fig. 11. Inversion b in fact gives the result of the first inversion including the spatial mean, significantly

TABLE 3. Average heat content (°C).

Layers (m)	Model	Inversion a	Iteration
0–300	−0.091	−0.093	−0.083
300–1000	−0.166	−0.197	−0.165
1000–2000	−0.030	−0.069	−0.035
2000–3000	−0.0053	−0.040	−0.011
3000–4000	−0.0014	−0.024	−0.008

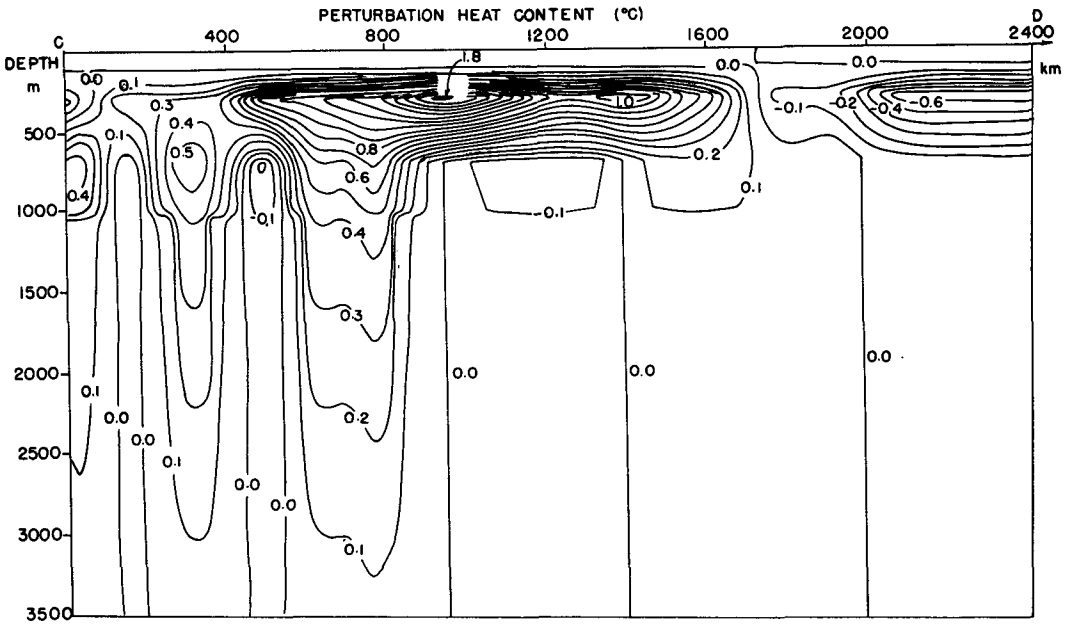

FIG. 12. Vertical slice of the perturbation heat content in °C along section CD at day 3606.

better than inversion a, carried out without the mean.

For section CD, the horizontal covariance function was still kept Gaussian, homogeneous and isotropic, as given by (20), but with 400 km width due to the shorter correlation lengths found along CD. The inclusion of the spatial mean makes the covariance function level off to the mean value of 0.5. (The total covariance is normalized with respect to the zero-lag value.)

For the inversion along CD and the successive iterations, different reference eigenrays traced through $C_0(z)$ were also used. The inverse can be shown to be rather insensitive to the type and number of used eigenrays as long as a good sampling is provided of the interior water mass (Malanotte-Rizzoli, 1984). The number of eigenrays for the following simulation was again kept at 6.

Figure 13 shows the average heat content vertical profile of section CD respectively from the model (continuous thick line); after the first inversion (broken line), after the first iteration (cross symbols), and after the second iteration (continuous thin line). The surface layer, down to a depth of ~200 m, is shaded; it is not sampled by the eigenrays.

The first inversion provides now an ocean which is too warm. Table 4 gives the warm biases after the first inversion versus the model values at different depths. As the section is more highly perturbed in the layer between 250 and 700 m, the highest warm biases are found there. We can compare the warm biases of Table 4 with the cold biases previously found for the cold section AB. Over the year 10 time evolution, the average cold bias at 300 m was approximately −0.025°C versus an average model value of −0.153°C. At 1000 m, the average cold bias was about −0.035°C versus the model value of −0.210°C. It is clear from Table 4 that the biases do not increase linearly with the average perturbation.

The continuous, thin line of Fig. 13 gives the average profile after the second iteration. Clearly, the iteration process provides a good estimate of the mean profile though the field is highly perturbed. In all the simulations carried out, a percentage error in the differential travel times $(\delta T_i)_n$ less than 0.01% was reached in ~3 iterations.

The results of this section and the previous one show that the iteration process allows us to remove the cold or warm biases and that the final estimate of the average heat content at various depths is very good.

f. Estimating the average pycnocline slopes

The basic assumption of every stochastic inversion lies in the *a priori* knowledge of the statistics of the field, specified in the form of the covariance function. In an Eastern Pacific section like Kenyon's shown in Fig. 8a, the phenomenological evidence tells us that the most important feature of the field are the isopycnal slopes in the eastward direction, with the majority of the energy being in the mean and only minor mesoscale activity. Had we been in a section in the middle of the subtropical gyre like section CD we might have expected a trough in the zonal isopycnal slope with successive eastward rising.

We can build this knowledge into the covariance. The inversion is general enough to allow general

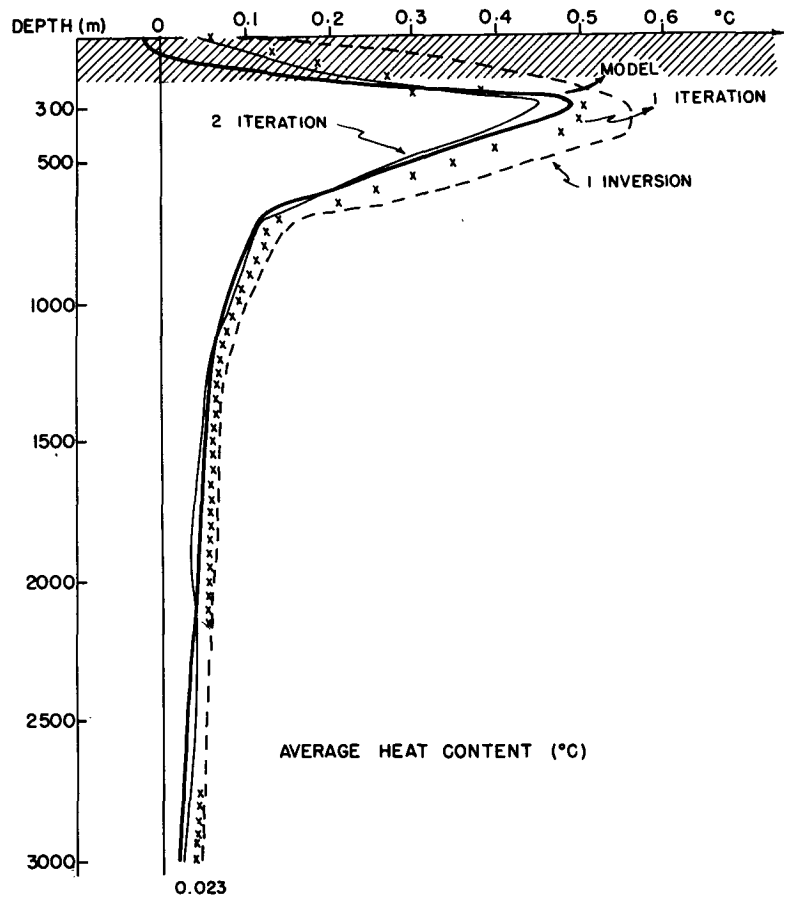

FIG. 13. Average heat content vertical profile along CD at day 3606 in °C. Model: continuous thick line. Result of the first inversion: broken line. Result after the first iteration: cross symbols. Result after the second iteration: continuous thin line. The shaded surface layer is not sampled by the acoustic rays.

shapes for the covariance, including inhomogeneous parts.

The simulations of this chapter are carried out again for section AB. We include an inhomogeneous covariance capable of reproducing the average isopycnal slopes observed along AB assuming a zonal dependence for the perturbation field given by

$$\delta C(x) = a(x - x_0 - b) \qquad (22)$$

where x is the eastward coordinate along AB, with the origin at A and a is the slope, x_0 is the *a priori* estimate of the zero-crossing location and b is the variation of the zero crossing around the *a priori* estimate x_0. In (22) a, b are random variables, assumed to be uncorrelated, and the zero-crossing location was given the value $x_0 = 6 \times 10^5$ m, near the eastern boundary A.

From (22) the inhomogeneous part of the covariance function is obtained and the total covariance for the two modes is

$$G(x_1, x_2) = H(r) + R(x_1, x_2)$$
$$= H(r) + \langle a^2 \rangle (x_1 - x_0)(x_2 - x_0) + \langle a^2 \rangle \langle b^2 \rangle \qquad (23)$$

with $H(r)$ the homogeneous part of the covariance. Equation (23) thus embodies the mesoscale covariance, the variance in the mean and the inhomogeneous covariance for the average slope. The variances of the slope and of the zero crossing location were assigned the following values: $\langle a^2 \rangle = 10^{-10}$ °C^2 m^{-2}; $\langle b^2 \rangle = 36 \times 10^{10}$ m^2. The estimate of the average

TABLE 4. Warm biases.

Depth (m)	Model $\delta\theta$ (°C)	Warm bias (°C)
300	0.490	+0.06
400	0.399	+0.16
500	0.304	+0.14
600	0.209	+0.12
700	0.112	+0.06
1000	0.085	+0.018
3000	0.020	+0.023

heat content along section AB after the first inversion is essentially identical to the estimate obtained carrying out the inversion with the covariance function including only the mean.

The effect of the inhomogeneous covariance $R(x_1, x_2)$ are clear when plotting the heat content spatial distribution along AB. Figures 14a and b show such distributions respectively for the 300 and 1000 m interfaces. The heat content spatial pattern (i.e. the pycnocline displacement) is shown only at the two model interfaces but is actually evaluated with the vertical resolution of 50 m. This gives the possibility of evaluating the vertical gradients of the slopes. With the inclusion of $R(x_1, x_2)$, the inversion is now capable of providing a remarkably good estimate of the average isopycnal slopes. For the 300 m interface, the inversion gives a mean slope estimate:

$$\hat{a}|_{300} = -1.82 \times 10^{-7} \text{ °C m}^{-1}$$

versus the model value

$$a|_{300} = -1.65 \times 10^{-7} \text{ °C m}^{-1}.$$

For the 1000 m interface, the estimated slope is

$$\hat{a}_{1000} = -1.36 \times 10^{-7} \text{ °C m}^{-1}$$

versus the model value

$$a_{1000} = -1.29 \times 10^{-7} \text{ °C m}^{-1}.$$

The inversion provides a horizontally continuous estimate of the two mode amplitudes $\delta\hat{C}_1(x)$, $\delta\hat{C}_2(x)$ discretized at 100 points along AB. The vertical structure is obtained multiplying each mode estimate through the corresponding climatological eigenmode. Thus the total sound speed perturbation field is given by

$$\delta\hat{C}(x, z) = \sum_{j=1}^{2} \delta\hat{C}_j(x) \cdot \overline{\delta C_j(z)}. \qquad (24)$$

The inversion is capable of reproducing the change in isopycnal slopes with depth. In agreement with the model, the estimated mean slope $\hat{a}$ is smaller at 1000 m, where the two eigenmodes $\overline{\delta C_j(z)}$ have opposite signs, than at 300 m where they have the same sign. The mean slope ratios from the inverse is:

$$\frac{\hat{a}|_{300}}{\hat{a}|_{1000}} \approx 1.34$$

versus the model value

$$\frac{a|_{300}}{a|_{1000}} \approx 1.29.$$

The above slope estimates appear to be very good. The importance of obtaining good mean slope estimates can hardly be overemphasized. The isopycnal slopes, estimated with a good vertical resolution and averaged in time, could be used for β-spiral calculations (Schott and Stommel, 1978). Thus, simple density tomography would provide a tool to evaluate the absolute velocity field and not only the geostrophic velocity shear.

The dotted lines in Figs. 14a and b give the result of the first iteration. At 300 m, where the energy level in the mean is greater, the first inversion itself provides a very good estimate of the mean heat content value. Thus, the heat content spatial distribution obtained from the first iteration oscillates around the average basic state. At 1000 m the mean value provided by the first inversion is −0.132°C versus the model value of −0.116°C. In the first iteration, when we tend to make the ocean "warmer," the heat content spatial distribution is shifted towards more positive values. The new mean after the first iteration is −0.123°C.

The above procedure can be generalized to any shape of the inhomogeneous covariance $R(x_1, x_2)$. For section CD in fact the inclusion of a parabolic covariance allows us to reproduce the 300 m interface characterized by the large pycnocline trough of the gyre interior (Malanotte-Rizzoli, 1984).

4. Conclusions

In this work a tomographic experiment has been simulated in a given model ocean over ranges as long as the gyre-scale. The purpose was to explore the potential of the tomographic technique to measure average quantities of importance for the general circulation and ocean climate.

The first step to address the above question is the simulation of the experiment in the model ocean to explore the potential of the experimental technique in measuring the desired quantities.

The focus of the present simulations of the tomographic experiment was upon the following quantities: 1) the vertical profile of heat content horizontally averaged along the tomographic section; 2) time-variability of the average heat content, or average pycnocline displacement, at different depths; 3) average pycnocline slopes at different depths along the tomographic section. The results and conclusions of the simulations can be summarized as follows.

(i) The inversion procedure as it was designed for the 1981 mesoscale experiment needs to be improved over ranges as long as the gyre-scale. The inversions provide an ocean which has cold or warm biases with respect to the true ocean. These are due to the nonlinear nature of the data and to the fact that the inversion is based upon linear estimation theory. The inversion can be implemented in the most straightforward way through an iteration process which relaxes the "frozen ray" assumption and reconstructs successive better approximations to the instantaneous perturbed ocean. The iteration process converges very fast, in 3–4 iterations at most, assuming as conver-

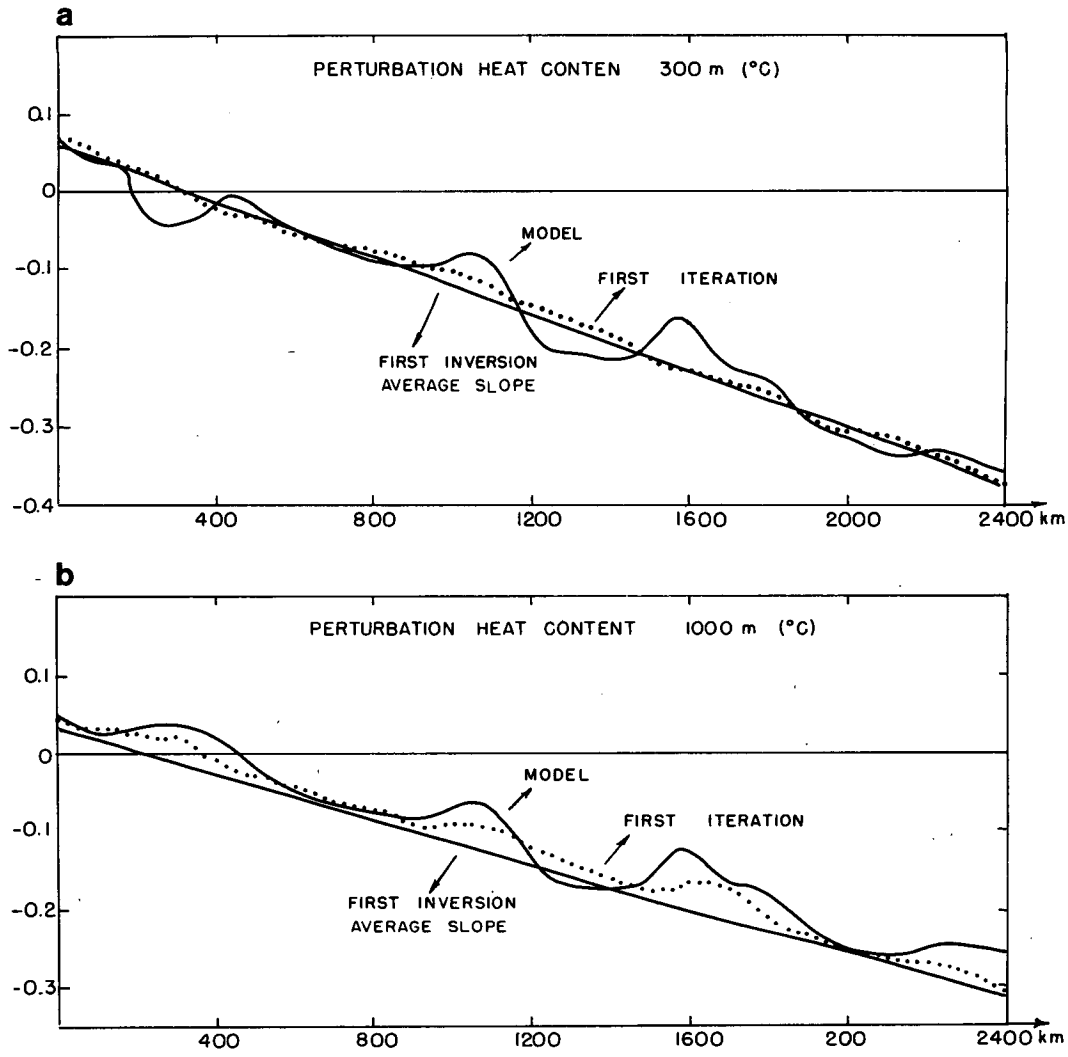

FIG. 14. (a) Interface at 300 m depth. Heat content spatial distribution along AB at day 3606. Model: continuous thick line. Also shown is the average slope after the first inversion using the inhomogeneous covariance (23) and the spatial distribution after the first iteration (dotted line). (b) As in (a) but for the interface at 1000 m depth.

gence criterion the fact that the data at the n-iteration have a percentage error below an assigned value ϵ.

(ii) Through iteration, warm and cold biases are removed. The consequent estimates of the average heat content at different depths, in the layer sampled by the chosen eigenrays, are shown to be very good. The accurate estimate of the average heat content is shown to hold for sections having relatively high sound speed perturbations, of the order of ~ 10 m s^{-1}. Higher perturbation values seem to be rather improbable for the Eastern Pacific which has been shown to be nearly void of mesoscale activity.

(iii) Through a time evolution experiment carried out for the duration of a full year the average pycnocline displacement time evolution can be monitored at various depths. Thus tomography can measure the frequency spectrum of the average pycnocline displacement in layers below the surface mixed layer in which the circulation is basically wind-driven.

(iv) The inversion is general enough to accept inhomogeneous covariance functions. In regions of the ocean in which the major feature of the pycnocline are long-scale trends, like average slopes, the inclusion of an inhomogeneous covariance for the slope allows us to reproduce these trends. Thus, average pycnocline slopes over the tomographic section can be measured very accurately with good resolution all over the water column.

Acknowledgments. This research was carried out with the support of the National Science Foundation, Grant OCE-8214821. Thanks are due to Ms. Isabelle Kole who expertly drafted the figures and Ms. D. L. Frank who carefully typed the manuscript.

APPENDIX A

Interpolation Procedure

Two types of interpolation are required, the first to reconstruct the sound speed perturbation field and, hence, the total sound speed field in each perturbed realization of the model ocean. The second interpolation provides the climatological first and second baroclinic eigenmodes for the sound speed perturbation $\overline{\delta C_1}$, $\overline{\delta C_2}$ to be used in the inversion.

The reconstruction of the sound speed field bears upon passing from the model 3-layered version to a vertical resolution capable of approximating the continuous representation given by (7a, b, c). Thus, the streamfunction field ψ is directly interpolated. The following conditions are used.

(i)
$$\psi = \psi_1 \quad \text{at} \quad z_1 = -150 \text{ m}$$
$$\psi = \psi_3 \quad \text{at} \quad z_2 = -650 \text{ m}$$
$$\psi = \psi_5 \quad \text{at} \quad z_3 = -3000 \text{ m}, \qquad \text{(A1)}$$

the three-layer values at each layer intermediate depth.

(ii) The model interfaces are known:

$$\zeta_2 = -h_2 = -\frac{f_0}{g_2'}(\psi_1 - \psi_3) \text{ at } z = -H_2 = -300 \text{ m}$$
$$\zeta_4 = -h_4 = -\frac{f_0}{g_4'}(\psi_3 - \psi_5) \text{ at } z = -H_4 = -1{,}000 \text{ m} \qquad \text{(A2)}$$

with $f_0 = 9.3 \times 10^{-5}$ s^{-1}; $g_2' = 0.03$ m s^{-2}; $g_4' = 0.013$ m s^{-2}. To respect the condition that the sound speed perturbation field—or, equivalently, the perturbation heat content—is the "mirror image" of the pycnocline displacement, the displacements ζ_2, ζ_4 are assigned in the interpolation. Specifically, from (7b):

$$\frac{-f_0}{N^2(z)}\psi_z = \begin{cases} \zeta_2 & \text{at} \quad z = -H_2 \\ \zeta_4 & \text{at} \quad z = -H_4. \end{cases} \qquad \text{(A3)}$$

Expression (A3) for ψ_z involves the proportionality factor $N^2(z)/f_0$, depending on the local Brunt-Väisälä frequency. Average Brunt-Väisälä frequency profiles exhibit maxima of ~3 cycles/hour at depths in the range 500–1000 m (Pedlosky, 1979). For a Brunt-Väisälä frequency profile taken at weather station November in the Eastern Pacific, Emery and Magaard (1976) have values ranging between 1.7 and 2.9 cycles/hour in the layer between 300 and 1000 m. Thus, the following values were chosen in the model simulation:

$$N|_{z=-300\text{ m}} = 3.86 \times 10^{-3} \text{ rad s}^{-1} \approx 2.2 \text{ cycles/hour}$$
$$N|_{z=-1000\text{ m}} = 4.31 \times 10^{-3} \text{ rad s}^{-1} \approx 2.5 \text{ cycles/hour}.$$

(iii) The model is flat-bottomed but forced at the surface by the wind stress. This implies that the vertical velocity at the surface is not zero. Instead $w = w_E$, determined by Ekman pumping. However, the inversion procedure is cast in terms of the climatological eigenmodes $\overline{\delta C_1}$, $\overline{\delta C_2}$, derived from the baroclinic eigenmodes $\bar{\psi}_{1b}$, $\bar{\psi}_{2b}$ of the streamfunction field (see in the following). These, in the continuous representation, are solutions of the Sturm-Liouville problem (8). In the 3-layered representation, they are solutions of the discretized, 3-layered version of (8) (Flierl, 1978), with boundary conditions $\psi_z = 0$ at $z = 0, -H$. The inversion procedure will thus provide a sound speed perturbation field satisfying the condition $\delta C \propto \psi_z = 0$ at $z = 0, -H$. The condition of no vertical velocity at the top and bottom was therefore used in the reconstruction of the perturbed sound speed field:

$$\psi_z = 0 \quad \text{at} \quad z = 0, -H. \qquad \text{(A4)}$$

Using conditions (i), (ii), (iii) the streamfunction field ψ was vertically interpolated using cubic or quadratic spline fitting in the three successive vertical layers:

0–650 m; 650–3000 m; 3000 m–bottom

to avoid spurious fluctuations which might have resulted from fitting a unique spline throughout the depth. The interpolation was made with a grid-size $\Delta z = 50$ m, leading to a vertical resolution of 100 layers (101 ψ-points) over 5000 m depth. From

$$\frac{\delta C_p}{C_{0p}} = \frac{\alpha f_0}{g}\psi_z \qquad \text{(A5)}$$

the ratio $\delta C_p / C_{0p}$ is obtained through finite differences. Using the Eastern Pacific reference profile $C_0(z)$ shown in Fig. 5 the sound speed perturbation field (δC_p) is reconstructed and, consequently, the total perturbed sound speed field $C_p(\mathbf{x}) = C_{0p}(z) + \delta C_p(\mathbf{x})$, as given by (9).

Here a point must be noticed. The model ocean climatological pattern does not obviously correspond to the basic reference profile $C_0(z)$ of the Eastern Pacific. The climatological state itself constitutes a perturbation to $C_0(z)$. The basic reference profile consistent with the model climatological mean is then

$$\bar{C}(z) = C_0(z) + \overline{\delta C(z)} \qquad \text{(A6)}$$

with $\overline{\delta C(z)}$ the perturbation in the climatological mean reconstructed from (A5) as previously described, and horizontally averaged over the eastern-ocean continuous box of Fig. 4. However, the perturbation sound speed field in the climatological mean is very small, particularly in the rather quiescent eastern region of the model ocean. Thus, the reference profile $\bar{C}(z)$ given by (A6) is practically identical to $C_0(z)$.

A second interpolation is required to obtain the first and second average baroclinic eigenmodes $\overline{\delta C_1}(z)$, $\overline{\delta C_2}(z)$ for the sound speed perturbation field. These are evaluated from (A5) through finite differ-

ences once the first and second baroclinic eigenmodes for the streamfunction ψ have been obtained. The eigenmodes $\bar{\psi}_{1b}$, $\bar{\psi}_{2b}$ are evaluated from the climatological 20-year mean and horizontally averaged over the eastern ocean box of Fig. 4, to represent a climatological as well as space average. To obtain the mode coefficients from the model, the problem to be solved is the 3-layered version of the continuous Sturm-Liouville problem (8), namely (Flierl 1978):

$$\frac{f_0^2}{\epsilon_{i-1}gH_i}(F_j^{i-1} - F_j^i) - \frac{f_0^2}{\epsilon_i gH_i}(F_j^i - F_j^{i+1}) + \lambda_j F_j^i = 0 \quad \text{(A7)}$$

with $i = 1, 2, 3$ for the 3 model layers; F_j^i is the amplitude of the jth normal mode in the ith layer; $\epsilon_i = (\rho_i - \rho_{i+1})/\rho_0$ are the reduced gravities for each layer. The boundary conditions of zero vertical derivative ψ_z at the top and bottom are implicit in the definition:

$$\epsilon_0 = \epsilon_3 = \infty.$$

Solution of the system (A7), through the condition that the determinant must vanish, leads to the three eigenvalues:

$$\lambda_1 = 0 \quad \text{infinite barotropic Rossby radius,}$$

$$\lambda_2 = 6.062 \times 10^{-10}$$

$$R_2 = (1/\lambda_2)^{1/2} = 40.616 \text{ km}$$

first baroclinic Rossby radius,

$$\lambda_3 = 18.834 \times 10^{-10}$$

$$R_3 = (1/\lambda_3)^{1/2} = 23.042 \text{ km}$$

second baroclinic Rossby radius. (A8)

Solution of (A7) for each mode with its eigenvalue λ_j, leads to the evaluation of the modal amplitudes in each layer. The barotropic mode amplitudes are identical in the three layers. For the baroclinic modes $j = 2, 3$ (A7) gives the ratios of the mode amplitudes in two layers with respect to the mode amplitude in the third layer. Use is made of the normalization condition:

$$\frac{1}{H}[H_1(F_j^1)^2 + H_2(F_j^2)^2 + H_3(F_j^3)^2] = 1; \quad \text{(A9)}$$

thus obtaining the mode amplitudes in each layer. Here $F_1^1 = F_1^2 = F_1^3 = 1$ for the barotropic mode. In matrix notation, we can write:

$$\mathbf{MA} = \psi \quad \text{(A10)}$$

where

$$\mathbf{A} = \begin{vmatrix} a_1 \\ a_3 \\ a_5 \end{vmatrix}$$

is the vector of the mode amplitudes;

$$\psi = \begin{vmatrix} \psi_1 \\ \psi_3 \\ \psi_5 \end{vmatrix}$$

is the vector of the streamfunction values in each layer. The matrix **M** thus provides the contributions of each mode to the total streamfunction value ψ_i in each layer. The inverse problem:

$$\mathbf{A} = \mathbf{M}^{-1}\psi \quad \text{(A11)}$$

allows us to find the mode amplitudes a_i as linear combinations of the streamfunction values ψ_i. The $\mathbf{M}^{-1}$, normalized with respect to the streamfunction weight in the second layer, is:

$$\mathbf{M}^{-1} = \begin{vmatrix} 0.4286 & 1 & 5.7143 \\ 1.161 & 1 & -2.161 \\ 0.4465 & -1 & 0.5535 \end{vmatrix}. \quad \text{(A12)}$$

In the matrix **M** the percentages of the two baroclinic modes in each layer are also normalized with respect to the mode percentage in the second layer according to the zero-vertical transport condition:

$$\alpha_1 H_1 + \alpha_2 H_2 + \alpha_3 H_3 = 0 \quad \text{(A13)}$$

where α_1, α_2, α_3 are the percentages of the considered baroclinic mode in layers 1, 2, 3. For the first baroclinic mode:

$$\frac{\alpha_1}{|\alpha_2|}\frac{H_1}{H_2} = 1.161; \quad \frac{\alpha_3}{|\alpha_2|}\frac{H_3}{H_2} = -2.161.$$

For the second baroclinic mode

$$\frac{\alpha_1}{|\alpha_2|}\frac{H_1}{H_2} = 0.4465; \quad \frac{\alpha_3}{|\alpha_2|}\frac{H_3}{H_2} = 0.5535.$$

With this normalization, the matrix **M** is

$$\mathbf{M} = \begin{vmatrix} 1 & 2.709 & 1.042 \\ 1 & 1 & -1 \\ 1 & -0.378 & 0.097 \end{vmatrix}. \quad \text{(A14)}$$

From the evaluation of the mode amplitudes a_1, a_3, a_5 provided by (A11) the matrix **M** gives the modal shapes and the percentage of each mode in each layer with respect to the streamfunction total value. Then the modal amplitudes are known at $z_1 = -150$ m; $z_2 = -650$ m; $z_3 = -3000$ m. Using the zero vertical velocity condition $\psi_z = 0$ at $z = 0, -5000$ m, the vertical interpolation is carried out in a completely analogous way to the one previously described (cubic or quadratic spline fitting in 3 successive vertical layers), with the vertical discretization $\Delta z = 50$ m leading to the resolution of 100 vertical layers.

APPENDIX B

Inversion Procedure

The matrix $\mathbf{D}^T \equiv \{D_1, \ldots, D_n\}$ is the vector of travel time perturbations:

$$D_i \equiv \delta T_i = (T_i)_{\text{pert}} - T_{i0} \tag{B1}$$

with T_{i0} given by (13) and $(T_i)_{\text{pert}}$ given by (14) for the nonlinear direct problem. Alternatively (δT_i) can be evaluated as in (16), the linearized direct problem. We want to construct a linear estimator of $\delta C(\mathbf{x})$ from the data δT_i. At every point $\mathbf{x}$:

$$\delta\hat{C}(\mathbf{x}) = \sum_{i=1}^{n} a_i(\mathbf{x})\delta T_i \tag{B2}$$

if n = number of data δT_i. The estimation is optimized so as

$$\langle|\delta\hat{C}(\mathbf{x}) - \delta C(\mathbf{x})|^2\rangle = E^2 = \text{minimum}$$

where $\delta C(\mathbf{x})$ is the "true" field. Thus, the a_i are calculated by minimizing

$$\langle|\sum_{i=1}^{n} a_i(\mathbf{x})\delta T_i - \delta C(\mathbf{x})|^2\rangle \tag{B3}$$

at each $\mathbf{x}$. By the Gauss-Markov theorem the matrix of $a_i(\mathbf{x})$ is given by:

$$A(\mathbf{x}) = \langle\delta C(\mathbf{x})\mathbf{D}^T\rangle(\langle\mathbf{D}\mathbf{D}^T\rangle)^{-1}$$
$$= \langle\delta C(\mathbf{x})\delta\mathbf{T}_i^T\rangle(\langle\delta\mathbf{T}_i\delta\mathbf{T}_j^T\rangle)^{-1}. \tag{B4}$$

The model-data covariance matrix $\langle\delta C(\mathbf{x})\delta\mathbf{T}_i^T\rangle$ and the data–data covariance matrix $\langle\delta\mathbf{T}_i\delta\mathbf{T}_j^T\rangle$ are evaluated using the linearized direct problem:

$$\delta T_i = -\int_{\Gamma i0} \frac{\delta C(\mathbf{x})}{C_0^2(z)}\, ds + (\epsilon_i + \delta_i) \tag{B5}$$

where ϵ_i is physical noise in the data, due to smaller-scale disturbances, and δ_i is measurement error. The error is assumed to have zero ensemble average $\langle\epsilon_i + \delta_i\rangle = 0$ and to be uncorrelated with the sound speed fluctuations. Using (B5) the model-data and data-data covariance matrices become

$$\langle\delta C(\mathbf{x})\mathbf{D}^T\rangle = \langle\delta C(\mathbf{x})\delta\mathbf{T}_i^T\rangle = \int_{\Gamma i0} \frac{\langle\delta C(\mathbf{x})\delta C(\mathbf{x}')\rangle}{C_0^2(\mathbf{x}')}\, ds$$
$$\langle\mathbf{D}\mathbf{D}^T\rangle = \langle\delta\mathbf{T}_i\delta\mathbf{T}_j^T\rangle = \int_{\Gamma i0}\int_{\Gamma j0} \frac{\langle\delta C[\mathbf{x}'(s')]\delta C[\mathbf{x}''(s'')]\rangle}{C_0^2[\mathbf{x}'(s')]C_0^2[\mathbf{x}''(s'')]}\, ds'ds'' + \gamma_{ij} \tag{B6}$$

with $\gamma_{ij} = \langle(\epsilon_i + \delta_i)(\epsilon_j + \delta_j)\rangle$ the total error covariance. The covariance matrix $\langle\delta C(\mathbf{x}')\delta C(\mathbf{x}'')\rangle$ is then specified as in (18). The error is evaluated from the inversion procedure. In matrix notation, (B2) can be written:

$$\mathbf{D} = \delta\mathbf{T}_i = \mathbf{G}\delta\mathbf{C} + \epsilon$$
$$\delta\hat{\mathbf{C}} = \mathbf{A}\mathbf{D}. \tag{B7}$$

The error covariance matrix is therefore

$$\langle\epsilon\epsilon^T\rangle = \langle(\delta\hat{\mathbf{C}} - \delta\mathbf{C})(\delta\hat{\mathbf{C}} - \delta\mathbf{C})^T\rangle$$
$$= \langle\mathbf{C}\delta\mathbf{C}^T\rangle - \langle\delta\hat{\mathbf{C}}\delta\mathbf{C}^T\rangle - \langle\delta\mathbf{C}\delta\hat{\mathbf{C}}^T\rangle + \langle\delta\hat{\mathbf{C}}\delta\hat{\mathbf{C}}^T\rangle$$
$$= \mathbf{R} - \mathbf{A}\langle\mathbf{D}\delta\mathbf{C}^T\rangle - \langle\delta\mathbf{C}\mathbf{D}^T\rangle\mathbf{A}^T + \mathbf{A}\langle\mathbf{D}\mathbf{D}^T\rangle\mathbf{A}^T \tag{B8}$$

where with $\mathbf{R}$ we indicate the covariance matrix of the sound speed perturbation field. But

$$\left.\begin{aligned}\mathbf{A} &= \langle\delta\mathbf{C}\mathbf{D}^T\rangle(\langle\mathbf{D}\mathbf{D}^T\rangle)^{-1} = \mathbf{P}\mathbf{Q}^{-1}\\ \mathbf{P} &= \langle\delta\mathbf{C}\mathbf{D}^T\rangle\\ \mathbf{Q} &= \langle\mathbf{D}\mathbf{D}^T\rangle\end{aligned}\right\}$$

$$\langle\epsilon\epsilon^T\rangle = \mathbf{R} - \mathbf{P}\mathbf{Q}^{-1}\mathbf{P}^T - \mathbf{P}\mathbf{Q}^{-1}\mathbf{P}^T$$
$$+ \mathbf{P}\mathbf{Q}^{-1}\mathbf{Q}(\mathbf{Q}^{-1})^T\mathbf{P}^T = \mathbf{R} - \mathbf{P}\mathbf{Q}^{-1}\mathbf{P}^T$$

as $(\mathbf{Q}^{-1})^T = \mathbf{Q}^{-1}$. Thus

$$\langle\epsilon\epsilon^T\rangle = \mathbf{R} - \mathbf{A}\mathbf{P}^T. \tag{B9}$$

The error variance for $\delta\hat{C}$ is given by the diagonal elements of the error covariance matrix (B9).

A noise level must be specified in (B5) embodying all sources of possible error. Assuming perfect data, namely $(\epsilon_i + \delta_i) \equiv 0$ can be troublesome for the inversion procedure if the inversion matrix is nearly singular. In this case, the typical effect of reducing the noise level is to overamplify the $\delta\hat{C}$ amplitudes estimated by the inverse. In the present modeling simulation, the noise level should parameterize the physical noise we want to filter out, i.e. the mesoscale signal. On ranges as long as those here considered (2400 km) the mesoscale activity can be qualitatively thought of as the analogous to the internal wave signal in the 1981 mesoscale experiment. In the latter case, the physical noise was assumed to be 0.005 sec for the travel time perturbations δT_i, over ranges of 300 km. Over ranges of one order of magnitude bigger, the physical noise error was assumed to be ϵ_i = 0.05 sec for the inversions discussed in Section 3c (Time evolution). The magnitude of the signal at the receiver is given by the diagonal elements of the matrix $\mathbf{Q} = \langle\delta\mathbf{T}_i\delta\mathbf{T}_j^T\rangle$ in (B6). With the above value for ϵ_i, signal-to-noise ratios for the six eigenrays used in the inversions varied in the range 20–26.

REFERENCES

Bernstein, R. L., and W. B. White, 1977: Zonal variability in the distribution of eddy energy in the midlatitude North Pacific Ocean. *J. Phys. Oceanogr.*, **7**, 123–126.

Cornuelle, B., 1983: Inverse methods and results from the 1981 Ocean Acoustic Tomography Experiment. Ph.D. dissertation, MIT/WHOI, 359 pp.

——, and Collaborators, 1984: Tomographic maps of ocean mesoscale. Part 1: Pure Acoustics. *J. Phys. Oceanogr.*, (in press).

Emery, W. J., and L. Magaard, 1976: Baroclinic Rossby waves as inferred from temperature fluctuations in the Eastern Pacific. *J. Mar. Res.*, **34**, 365–385.

Flierl, G. R., 1978: Models of vertical structure and the calibration of two-layer models. *Dyn. Atmos. Oceans*, **2**, 341–381.

Holland, W. R., 1978: The role of mesoscale eddies in the general circulation of the ocean. Numerical experiments using a wind-driven quasi-geostrophic model. *J. Phys. Oceanogr.*, **8**, 363–392.

Kenyon, K. E., 1983: Sections along 35°N in the Pacific. *Deep-Sea Res.*, **30**, 349–369.

Malanotte-Rizzoli, P., 1985: Long-range inversions for ocean acoustic tomography. *J. Geophys. Res.*, (in press).

Munk, W. H., and C. I. Wunsch, 1979: Ocean acoustic tomography: A scheme for large scale monitoring. *Deep-Sea Res.*, **26A**, 123–160.

——, and ——, 1982: Up/down resolution in ocean acoustic tomography. *Deep-Sea Res.*, **29**, 1415–1436.

Ocean Tomography Group, 1982: A demonstration of ocean acoustic tomography. *Nature*, **299**, 121–125.

Pedlosky, J., 1979: *Geophysical Fluid Dyunamics*. Springer-Verlag, 624 pp.

Schott, F., and H. Stommel, 1978: Beta spirals and absolute velocities in different oceans. *Deep-Sea Res.*, **25**, 961–1010.